



Design of a stiff and lightweight 5-Link SCARA robot

Master's Internship Project - Q1 2024

**Design for Precision Engineering
Control Systems Technology
Mechanical Engineering
&
Nobleo Technology**

Full Name	Student ID
Victor Suciu	1555650

Supervisors

Kees Verbaan
Patrick Houben

Frank Sperling
Joey Verest

Eindhoven, December 6, 2024

Abstract

The design and evaluation of a stiff and lightweight 5-link SCARA robot aimed at high-precision, high-throughput semiconductor applications is presented in this work. The project investigates the feasibility of a double SCARA topology to meet stringent accuracy, speed, and dynamic requirements while taking advantage of the potential benefits of the reduced moving mass. The design methodology incorporates performance metrics such as encoder sensitivity, conditioning, and motor torque, all optimized using a non-dimensional kinematic analysis method. Findings suggest that a degenerate SCARA with co-axial motors provides optimal performance under the specified requirements. The detailed conceptual design, including static accuracy and dynamic performance considerations, demonstrates the capability of this robot architecture. The joints between the links of the robot are designed such that the end effector is exactly constrained by the parallel manipulator. Several Computer Aided Engineering tools from the SOLIDWORKS package were employed to evaluate the dynamic performance of the system.

Contents

1 Introduction	1
1.1 SCARA basics	1
1.2 Literature review	2
1.2.1 The FAMM	3
1.3 Proposed design workflow	3
2 Optimal Robot Synthesis	4
2.1 Assumptions	4
2.2 Performance atlas method overview	5
2.3 Performance index definitions	7
2.3.1 Global conditioning index	7
2.3.2 Transmission angle deviation	8
2.3.3 Rectangle width	8
2.3.4 Encoder sensitivity	9
2.3.5 Stiffness index	10
2.3.6 Motor torque	11
2.4 Optimum atlas overlap and selection	12
3 Conceptual Design	15
3.1 Requirements	15
3.1.1 On the required accuracy and dynamics	15
3.2 Functional breakdown	16
3.2.1 End effector position sensing	16
3.2.2 Torque supply	17
3.2.3 End effector rotation coupling	17
3.2.4 End effector volume integration	18
3.2.5 Wrist joint connection	18
3.2.6 Floating link stiffness & mass	21
3.2.7 Elbow joint connection	22
3.2.8 Driven link stiffness & mass	23
3.2.9 Shoulder joint connection	23
3.2.10 Bearing selection	25
3.3 Design embodiment	26
3.3.1 Links	27
3.3.2 Wrist joint	27
3.3.3 Elbow joints	28
3.3.4 Shoulder joints	28
3.4 Evaluation	29
3.4.1 Modal analysis	29
3.4.2 End effector stiffness	32
3.4.3 Motor torque	32
4 Conclusion	33
5 Recommendations	34
References	35
A Length set local performance plots.	37
B Additional FEM results	41
B.1 Mesh quality	41
B.2 Erroneous modes	41
B.3 Modes 2-9 for the front-right pose	42

1 | Introduction

Nobleo Technology was tasked by a client to design a pick & place machine that acts as a component supply for one of the client's existing machines. The machine to be designed must pick IC dies from a series of tape reels and feed them into the client's machine via a shuttle stage that moves into the client's machine space through an opening in its side (as depicted in Figure 1.1). In order to bridge the gap between the tape reels and the shuttle, some sort of robotic manipulator is required. The robotic manipulator must be able to move in a limited rectangular workspace and accurately position the picker head connected to its end effector over the required locations. Assuming that the vertical motion required to pick up the dies, retract during movements and drop off the dies on the shuttle is integrated into the picker, the robotic manipulator must then only move in 2D. During the incipient phase of the project, Nobleo considered multiple possible concepts for this planar manipulator. One of the concepts was a double SCARA robot, which appeared promising due to its potential for a low-mass, fast-moving, design. In the end, the SCARA concept was dropped in favor of a more standard cartesian manipulator, on the basis of technology readiness, given that market research showed no existing applications of such robots in the semiconductor industry (at least in this role).

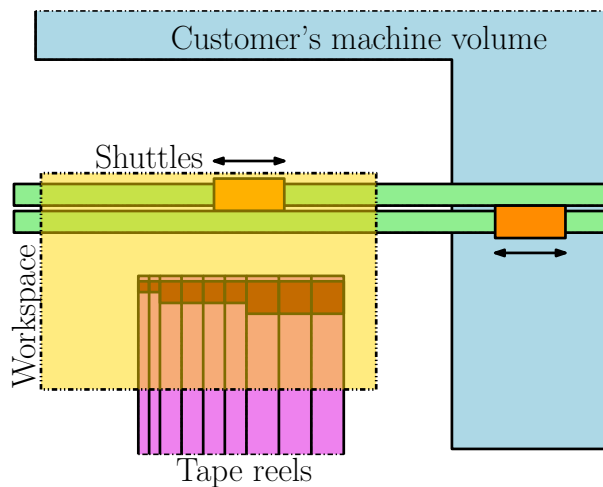


Figure 1.1: Schematic representation of the design challenge. The pick and place cycles are executed between the shuttles (orange) and the outputs of the tape reels (red).

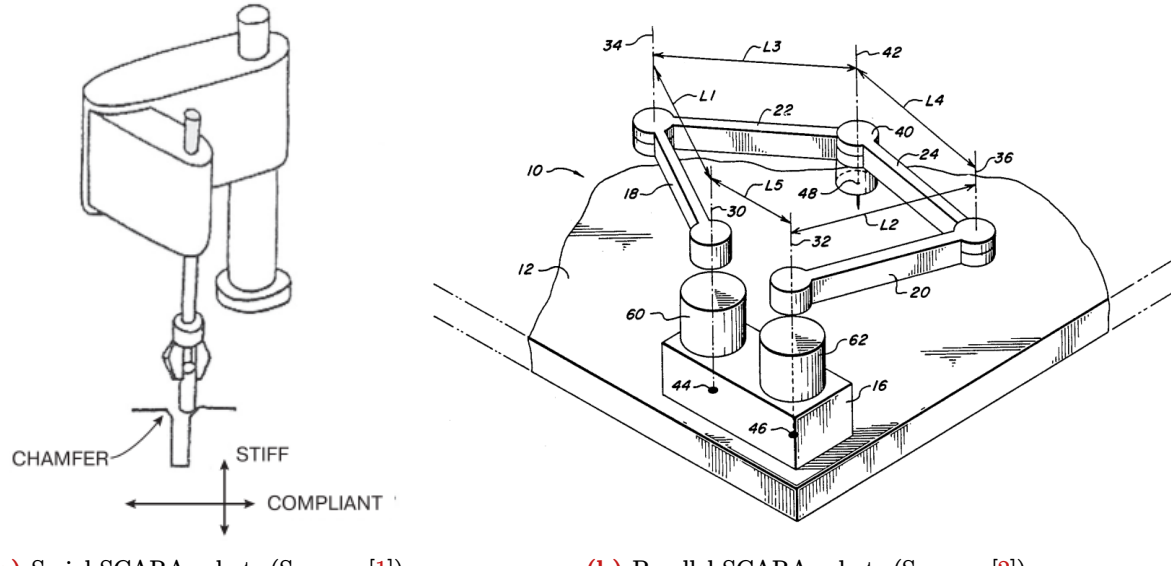
While Nobleo continues implementation of the cartesian stage for the client's machine, **the objective of this internship project is to investigate the feasibility of a double SCARA robot in a high-precision, high-throughput, semiconductor application**, with the ultimate goal of enabling the realization of a demonstrator prototype and answering the question "Is there a good reason that double SCARA robots are not widely used in the industry?". Even though the robot is not intended to replace the one in Nobleo's project, the same set of requirements (see Table 3.1 for a full list) is taken, in order to enable a one-to-one comparison.

1.1 | SCARA basics

The first SCARA robot prototype was created in Japan, in 1978 [1]. The name stands for Selective Compliance Assembly Robot Arm, where selective compliance refers to the relative planar compliance of the positioning of the end effector, compared to its vertical stiffness [1]. This feature, which was fundamentally built-in to the design, allows for a slight miss-alignment of the end effector in the planar directions, which can be a useful trait in industrial assembly automation (the original application of the SCARA concept), such as when inserting a peg into a hole (see Figure 1.2a). The robot's topology resembles that of a human's arm, with a shoulder, elbow and wrist joint. Rotational motors at the shoulder and elbow allow positioning of the wrist in 2D space, while motors at the wrist joint can allow for orientation of the end effector (i.e. heading). Typically, when full 3D positioning is required, a vertical actuator is added at the wrist. This type of SCARA robot can be described as a serial SCARA, due to the series connection of the two positioning motors.

A *parallel* (or *double*) SCARA robot is a two-armed version of the SCARA concept that places both

planar positioning motors at the shoulder joints, on the fixed world. The second, floating, link of each arm is free to rotate in-plane, but by connecting the arms at the wrist, the free degree of freedom is constrained and the end effector can be positioned in 2D. Figure 1.2b shows a sketch of this robot topology, where 60 and 62 are the shoulder joints and 48 is the end effector. The connected arms form a so-called five-bar mechanism (where the fifth bar is the distance between the two shoulder joints), resulting in 5-bar SCARA and 5R SCARA being other names used for this type of robot. The main advantage of the parallel topology, compared to the serial one, is the potential reduction in moving mass by having both motors at the shoulders. This comes at the expense of the addition of a second moving arm, a typically more limited workspace and more difficult control due to the presence of kinematic singularities.



(a) Serial SCARA robot. (Source: [1])

(b) Parallel SCARA robot. (Source: [2])

Figure 1.2: Sketches of two different SCARA robot topologies.

1.2 | Literature review

The study of the kinematics of 5-bar SCARA robots is widely documented in literature. Many approaches to calculating the forward kinematics (coordinates of the end effector as a function of the positions of the motors) and inverse kinematics (positions of the motors as a function of the coordinates of the end effector) have been described, depending on the chosen coordinate system and angle notation [3–5]. The working modes of the robot are defined by the different solutions of the forward and inverse kinematics functions (i.e. the multiple solutions of an inverse trigonometric function) [5]. Typically, a working mode is chosen for the operation of the robot and the other solutions are disregarded [5]. Singularities are those poses of the robot where an instantaneous change of the mechanism's DoFs is encountered. They are a common occurrence in parallel mechanisms and pose an issue for control. The loss of DoFs causes the robot to effectively get stuck in a limited workspace unless an external force removes it from the singular configuration. It is therefore commonly chosen to restrict the workspace of the robot such that singularities are not encountered. Testing for singularities can be done through the velocity method [6], by calculating the determinant of the Jacobian matrix of the end effector, or via a geometric approach, using screw theory [7]. Gamble presents the development of a Python solver and simulator for 5-bar SCARA robots, together with some useful performance metrics, such as the error sensitivity to motor perturbations [3]. Demjen et al. describe an analytical formula that can be used to synthesize the link lengths for a 5-bar SCARA robot for a given workspace size requirement [8]. This workspace is singularity-free and the resulting robot's kinematics are qualified on several performance indices including the global manipulability index, the global conditioning index and the global stiffness index, as also defined in [9]. Huang employs the use of a multi-variable optimization algorithm to optimize the link lengths of a 5-bar robot based on an overall dexterity index [6]. This index is defined as the ratio of the percentage of a reference workspace that can be theoretically covered by the robot and the percentage of singularities in the workspace. Liu et al. present a non-dimensional analysis method where the design space for the choice of link lengths is collapsed onto a 2D trapezoid [5]. This trapezoid is then split into regions bounded by singularity behavior and global performance metrics are overlayed on top. This work is continued in [9],

where more metrics are presented and the overlap is used to determine the optimal link length ratio. This approach was originally proposed by [10], however this work does not consider the singularities as bounds for the usable workspace.

1.2.1 | The FAMM

The Fast and Accurate Manipulator Module is a SCARA robot concept developed between 1985-1990 at Philips CFT (Centrum voor Fabricagetechnologie = Center for Industrial Technology) by Rien Koster and Herman Soemers. It featured a parallel SCARA design with coaxial shoulder joints and was able to reach an accuracy of $\pm 50 \mu\text{m}$ [11]. In 1994, Denis Schipper defended his PhD thesis on the design of the Mobile Autonomous Robot Twente (MART) using the FAMM manipulator [12]. That version of the FAMM robot can be seen in Figure 1.3. Later on, Phillips CFT developed the FAMMDD, a direct drive version of the FAMM robot that replaces the original geared drivetrain [11]. Eventually, around 2002, the FAMMDD prototype ended up in the TU/e Control laboratory, where several MSc theses are executed on its control design [13–15]. In 2011, Herman Soemers publishes the Design Principles for Precision Mechanisms book, including a section that uses the FAMM as an example of exactly constrained design [16].

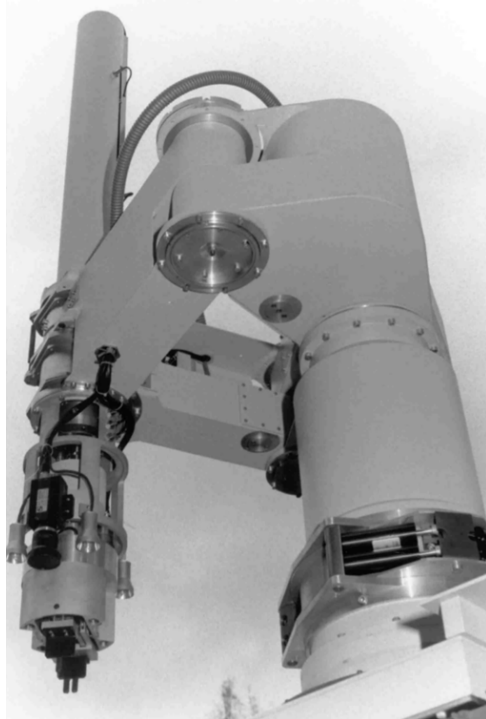


Figure 1.3: The FAMM manipulator, as integrated on the MART. (Source: [12])

1.3 | Proposed design workflow

The dynamic performance of a 5-bar SCARA robot is strongly dependent on its highly nonlinear kinematics. Therefore, in order to design a robot suitable for the desired high-speed, high-accuracy application, a comprehensive analysis of the kinematic design should be considered first. The optimal set of link lengths can then be selected, such that multiple performance metrics are maximized. This is done in section 2, using the atlas method presented in [5, 9]. Following the choice of link lengths, a functional breakdown of the design requirements can be made and the detailed design of each component can be realized in CAD, as shown in section 3. The performance of the design can then be evaluated using various computer-based methods, including finite element analysis.

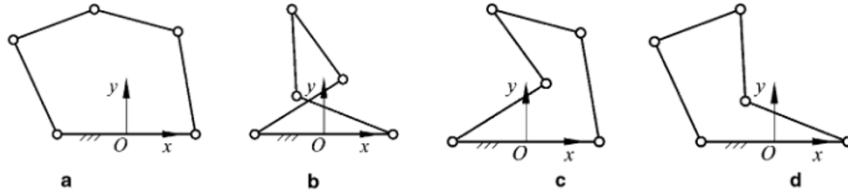
2 | Optimal Robot Synthesis

By employing the performance atlas method further described in [subsection 2.2](#), the performance of all possible link length ratios are evaluated. This allows for the selection of the optimal set of lengths, based on a number of different metrics, which acts as a foundation for the creation of the detailed robot concept.

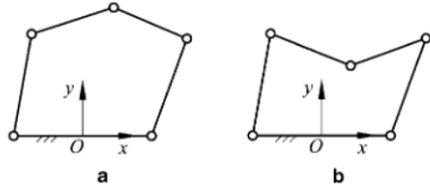
2.1 | Assumptions

The following list includes the main assumptions that are made in order to simplify and streamline the kinematic design problem. Most assumptions are commonplace in the study of 5-bar SCARA robots and should result in no loss of optimality.

- **5-bar design** - The chosen robot topology is that of a 5-bar mechanism. The robot has two arms, each comprised of a driven link and a floating link. The driven links connect to the fixed world at the shoulder joints. The driven and floating links of each arm connect at their respective elbow joint. The floating links of the two arms connect at the wrist, where the end effector is also placed. The lengths of all five links are non-negative.
- **Symmetry** - It is assumed that the robot is symmetric, i.e. the lengths of the driven links and those of the floating links are equal, respectively. This is shown in literature to not be restricting optimality. Moreover, the distance between the wrist joint and the end effector is assumed to be zero. This has been shown to be the optimal choice when considering a symmetric manipulator and use case [6]. This results in three link lengths remaining, namely the driven link length, the floating link length and the motor link length (i.e. the distance between the shoulder joints).
- **Working mode** - The "+-" inverse kinematic working mode is selected, together with the up-configuration of the forward kinematics. This working mode is the one least likely to result in links passing through each other. Mathematically this does not pose an issue, however, realizing a physical system that has clearance such that the other working modes are satisfied would prove difficult. Similar analyses can be conducted for the seven other working mode combinations. An overview of the possible working modes can be seen in [Figure 2.1](#).
- **No traversing of singularities** - In order to ensure an attainable level of control difficulty, the workspace of the robot must not include singularities. Furthermore, sufficient distance from bordering singularities should be maintained at all points in the workspace, including its boundaries. This approach is widely used in the study of parallel mechanisms, with most of the aforementioned literature focusing on designing robots such that this criterion is met.
- **Notation** - Unless otherwise mentioned, the following notation will be used, as depicted in [Figure 2.2](#). M₁ and M₂ are the left and right shoulder joints, respectively (coinciding with the locations of the motors). R₁ and R₂ are the left and right elbow joints. P is the location of the wrist joint and end effector. θ_1 and θ_2 are the angles of the motors. μ_1 and μ_2 are the transmission angles between the driven and floating links. The origin of the 2D coordinate system is in the middle of the motor link and the x-axis is aligned with it. The length of the driven links is A. The length of the floating links is B. The distance between the origin and the motors is W (the length of the motor link is 2W).



The four inverse kinematic models: (a) “+ –” model; (b) “– +” model; (c) “– –” model and (d) “++” model.



The two forward kinematic models: (a) the up-configuration and (b) the down-configuration.

Figure 2.1: Working modes of a 5-bar mechanism. (Source: [5])

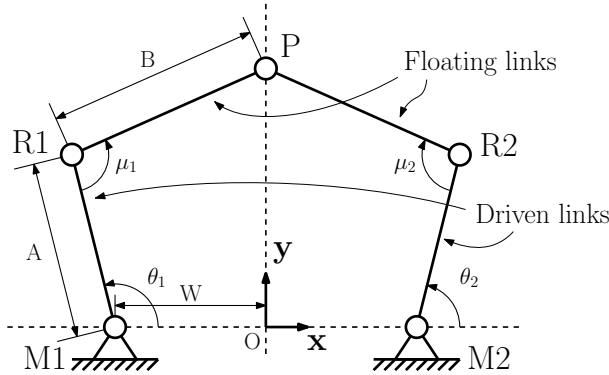


Figure 2.2: Notation used for the analysis of the 5-bar mechanism.

2.2 | Performance atlas method overview

The following section is a summary of the analysis method presented in [5, 9]. Following the original notations, the multi-dimensional space described by the link lengths as axes is referred to as *the design space*. The metrics used to evaluate the performance of the kinematic configurations are called *(performance) indices*. The charts used to plot the performance indices over the design space are referred to as *atlases*.

Taking into account the symmetry assumption, the design space is a three-dimensional space with axes going from zero to infinity (in line with the length of the respective link lengths). By calculating the average of the link lengths for a particular point (design) in the design space and using this average to normalize the link lengths, the axes of the design space become bound to the interval [0, 3]:

$$D = (A + B + W)/3 \quad (2.1)$$

$$a = A/D, \quad b = B/D, \quad w = W/D \quad (2.2)$$

$$\Rightarrow a + b + w = 3 \quad (2.3)$$

where a , b and w are the non-dimensional, normalized, link lengths. Taking into account the assembly constraint of $a + b \geq w$, as well as the fact that $a = 0$ or $b = 0$ would lead to singularities, results in the updated axis limits of:

$$0 < a, b < 3 \quad \text{and} \quad 0 \leq w \leq 1.5 \quad (2.4)$$

Applying Equation 2.3 to the 3D design space results in the design space collapsing to a 2D plane, as seen in Figure 2.3. Furthermore, applying the limits from Equation 2.4 bounds the design space to a trapezoid.

Following this process allows for the infinite 3D design space defined by A, B and W to be compressed to a 2D trapezoid defined by a, b and w, without loss of generality. That is because all kinematic performance metrics, and thus all indices that can be plotted in the trapezoid atlases, are entirely scale agnostic. Therefore, an optimal non-dimensional set of link lengths can be determined, which is then scaled up (or down) to match the dimensional requirements of the design, such as those for the workspace. From a kinematic perspective, the non-dimensional and the dimensional mechanisms are identical. However, the same cannot be said for dynamic performance indices, due to performance scaling non-linearly with the link lengths.

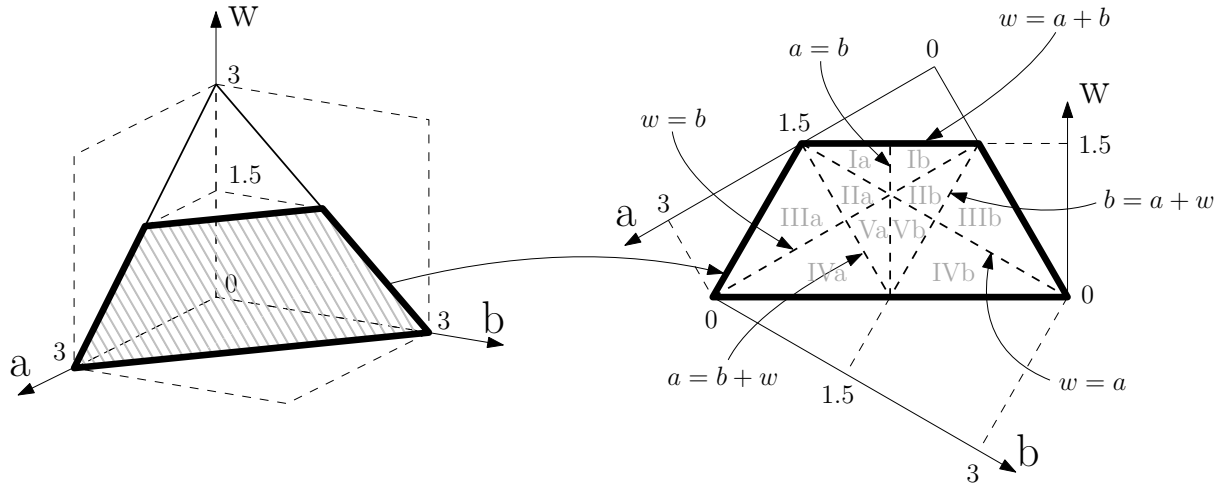


Figure 2.3: Visualizations of the non-dimensional design space. Left: 3D design space. Right: regions in the trapezoidal design space.

With the design space in the form of a trapezoid, it is now possible to further split it into regions bounded by identities between the coordinates, as depicted in Figure 2.3. These identities are relevant as they define which singularities show up in the workspace.

The *theoretical workspace* of a mechanism is defined as the planar region of space that the end effector can reach for a particular set of link lengths, ignoring any collisions between the links or the effect of singularities. Each arm of the robot defines its own reachable space similarly, namely that it is upper-bounded by the length of the arm in the extended configuration (both links aligned in extension) and lower-bounded by the length of the arm in the collapsed configuration (both links aligned, one over the other). These bounds form two annular regions, the intersection of which forms the theoretical workspace of the mechanism. The distribution of the theoretical workspace in the trapezoidal design space can be seen in Figure 2.4.

The singularities can also be overlayed on top of the theoretical workspace in order to reach a more realistic representation. Taking into account the choice for the "+-" working mode reduces the number of relevant singularities that occur for a particular mechanism. Furthermore, only the region of the workspace that is above the X axis is effectively usable in practice due to generally poor conditioning below it, as well as an increase in the number of poses where the links intersect for the aforementioned working mode. These singularities are depicted in Figure 2.4. Removing the bottom half of the workspace and only plotting the singularities for the chosen working mode drastically simplifies the plot and forms the *usable workspace*. Note that this step of selecting which singularities are to be plotted is not required in the numerical approach used in this work. That is because the local conditioning index (LCI) value at each pose is used to establish whether a pose is singular or not. If a singularity is to be relevant to the chosen working mode, then and only then will it show up in the plot of the LCI.

The overall shape of the usable workspace is defined by the region of the trapezoid design space that a design is in. Still, these shapes are generally non-uniform. A sub-section of the usable workspace must be chosen to act as the *actual workspace*. [5] introduces the concept of the maximal inscribed circle (MIC), which is the largest circular region bounded inside the usable workspace, to be used as the actual workspace. The advantage of using a circular region is that it can be analytically determined from the intersection of the relevant curves. The current work uses a rectangular region instead. This was chosen as it can more closely relate to the required rectangular workspace for the given application. For a given

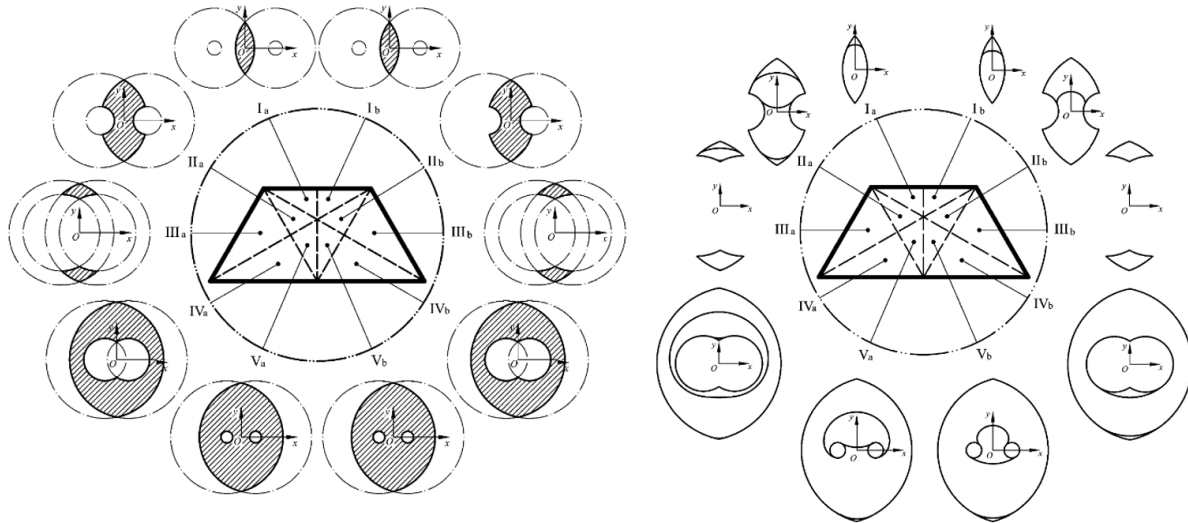


Figure 2.4: Visualizations of the different regions in the trapezoidal design space. Left: theoretical workspace. Right: Singularities present in the "+-" working mode. Note that the left and right side of the plots only start to differ once the working mode is selected. (Adapted from: [5])

aspect ratio, which converts the workspace requirement to a non-dimensional value, the largest inscribed rectangle can be found. The term *local index* refers to a performance index evaluated at a particular pose in the actual workspace of a particular robot design (e.g. local conditioning index LCI, which can be interpreted as how far away the current pose is from any singularity). A *global index* is the equivalent metric for the whole workspace, calculated by taking into account the contribution of all poses within the usable workspace, i.e. by averaging or taking the maximum value across the usable workspace (e.g. global conditioning index GCI, which can be interpreted as how much of the workspace is close to a singularity).

With the actual workspace region defined, global performance indices can be evaluated at each point in the design space. Plotting the values of a global performance index over the design space results in its atlas. Multiple atlases can then be computed for different indices. The regions where satisfactory values are found in each atlas can be overlapped to determine the optimal design (i.e. set of link length ratios). The link lengths are then scaled with the corresponding scaling factor, to bring the design back into the dimensional world, by bringing the actual workspace to the dimensions set by the requirement.

2.3 | Performance index definitions

The following sections describe the various performance indices used to qualify the performance of the possible robot link length ratios. For a set of link lengths, each index takes the form of a scalar value that says something about the behavior at a pose (for local indices) or across the entire actual workspace of the robot (for global indices).

2.3.1 | Global conditioning index

The conditioning index is the main performance metric implemented in this approach. It is useful as a numerical indicator for whether a particular pose of the robot is close to, or at, a singularity. The following relation can be used to link the velocities of the motors to those of the end effector:

$$\dot{\theta} = J\dot{p} \quad (2.5)$$

where $\dot{p} = (\dot{x} \ \dot{y})^\top$ is the vector of end effector velocities, $\dot{\theta} = (\dot{\theta}_1 \ \dot{\theta}_2)^\top$ is the vector of motor velocities and J is the Jacobian matrix of the mechanism. The condition number of the Jacobian matrix is defined as the ratio of its singular values and is a value larger or equal to 1.

$$\kappa_J = \sigma_1 / \sigma_s \quad (2.6)$$

The condition number can be used as a measure of the error introduced by numerical calculation of the inverse of a matrix [9]. The higher the condition number of the Jacobian is, the closer to a singularity

the robot is. Since this value is defined over $[1, \infty)$, it is more practical to consider its inverse. The local conditioning index is defined as:

$$LCI = 1/\kappa_J \quad (2.7)$$

The LCI can then be computed for a particular pose of a robot design. In order to ensure good controllability at the given pose, the value of the LCI should be maximized. A value of 0 indicates that the robot is in a singular pose. An example of an LCI plot can be seen in [Figure 2.5](#).

The global conditioning index can be defined as the integral of the LCI for all poses in the workspace times the area of the infinitesimally small element of the discretization, divided by the area of the workspace. In practice, since the area elements created by the discretization are equal in size, the GCI can be simplified to the average of the LCI taken at every point in the workspace.

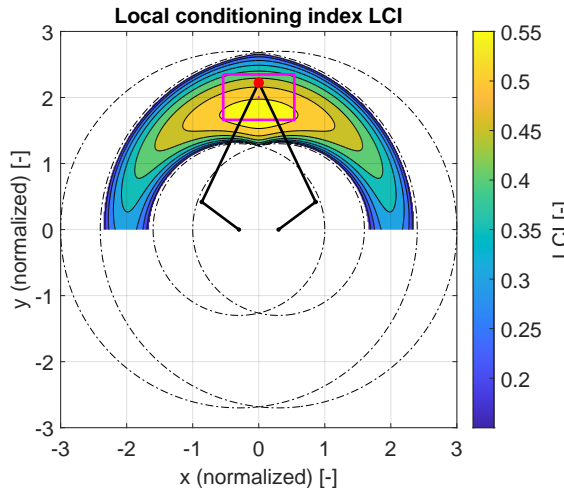


Figure 2.5: Plot of the LCI for a robot in region IVb. The corresponding robot is shown in black, at an arbitrary pose. The actual workspace is shown in magenta. The GCI for this robot is 0.52.

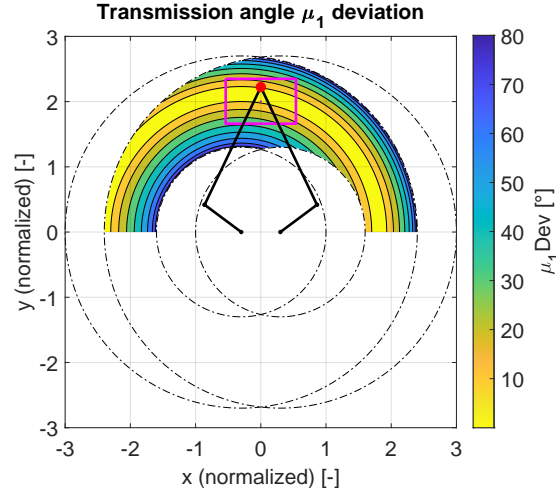


Figure 2.6: Plot of the μ_1 deviation for a robot in region IVb. The μ_1 DevMax for this robot is 38.2° and the μ_1 DevAvg is 19.0° . The plot for the other arm is symmetric.

2.3.2 | Transmission angle deviation

The transmission angles μ_1 and μ_2 of a SCARA robot are defined as the angles made by each floating link with respect to its corresponding driven link, as shown in [Figure 2.2](#). In order for an efficient force transfer from the motors to the end effector, the transmission angles should be close to 90° . A general rule of thumb is that the transmission angles should not vary more than $\pm 50^\circ$ [3].

The transmission angle deviation, muDev, is the absolute amount that the transmission angle of a robot at a particular pose deviates from a perfect 90° transmission. An example of a muDev plot can be seen in [Figure 2.6](#). This index can be evaluated over the robot workspace in two ways. The maximum of the muDev can be used to evaluate the worst case transmission angle that is encountered at some point in the workspace. The average of the muDev can be used as a measure of the overall quality of the transmission angles encountered.

2.3.3 | Rectangle width

In order to be able to calculate any of the global indices over the actual workspace of the robot, a method to determine the largest inscribed rectangle (of a given aspect ratio) within a region bounded by singularities must be implemented. The value of the LCI is used for this purpose. The following assumptions are made:

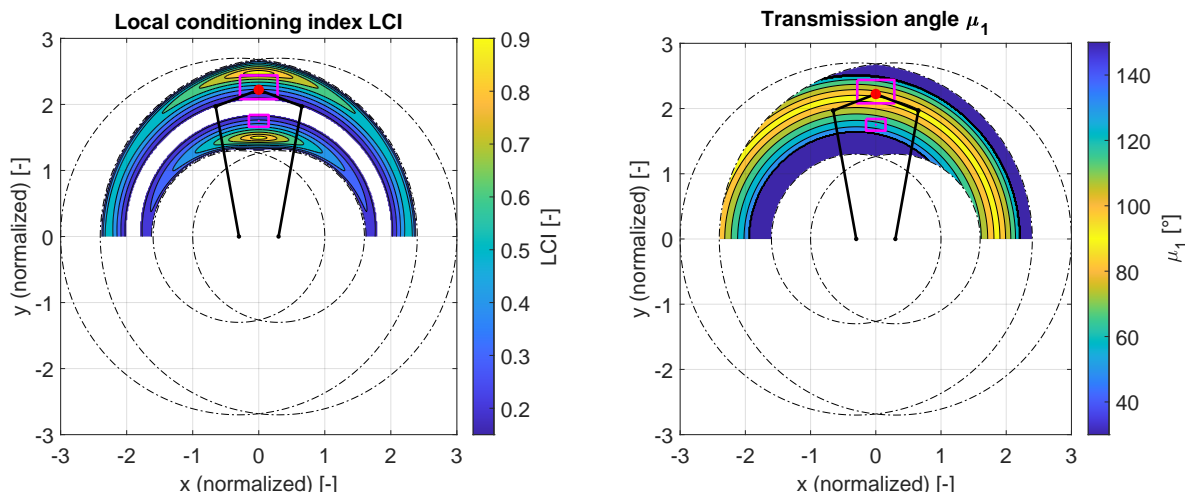
- The center of the largest inscribed rectangle is on the y-axis and the rectangle is aligned with the x- and y-axes (i.e. not oblique). While these assumptions are usually not true when looking for the absolutely largest inscribed rectangle within the usable workspace, they are true if a minimum level of quality of the workspace is required (i.e. a decent value for each of the other performance indices) within this rectangular selection of poses.

- Within a region bounded by singularities, the maximum rectangle width is convex. This implies that there are no local minima or maxima, there is only one maximum value and the minimum widths go to zero as the bordering singularities are approached.

The latter assumption allows for a ternary search algorithm [17] to be used to identify the optimal point on the y-axis to act as the center of the rectangle. The argument of the ternary search is the maximum width of a rectangle that can be inscribed and that has that particular point as its center. This maximum width is determined through a brute force approach where a rectangle is grown from the center point outwards until it reaches a stopping condition, which can be either of the following:

- The value of the LCI drops below 0.15. This value includes a sizable minimum margin to be maintained from singularities at all points in the selected workspace. If bordering singularities is not a consideration, a limit as low as 0.01 could be used [6].
- The transmission angle deviation exceeds a value of 40° . This requirement is added in order to ensure the enforcement of the muDev rule of thumb.

The rectangle returned by this process is the largest rectangle that can be inscribed within a region bounded by singularities in the theoretical workspace (and that satisfies the muDev rule of thumb) and can be used as the actual workspace of the robot. The example depicted in Figure 2.7 highlights a scenario with two regions divided by a singularity through the middle of the usable workspace. The algorithm returns the larger of the two rectangles. Note that some edges of the rectangles are defined by the LCI criterion, while others are defined by the transmission angle criterion.



(a) LCI plot. White band is caused by the mask applied to remove singularities. (b) μ_1 plot. Values outside of the $\pm 40^\circ$ range are set to 0.

Figure 2.7: Potential inscribed rectangles found in the usable workspace of a robot in region IVa. The corresponding robot is shown in black, at an arbitrary pose.

The rectWidth% index is defined as the ratio between the maximum inscribed rectangle width and the maximum envelope of the robot regardless of design, which in the non-dimensional design space is 6 ($= 2 \cdot 3 = 2 \cdot \max(a + b)$, coinciding with the width of the plots). This ratio is then the percentage of the total space allocated to the robot that is actually usable, in the form of workspace.

The scalingD index is calculated as the dimensional requirement for the workspace width divided by the non-dimensional rectangle width. This results in the scaling term D , as defined in Equation 2.1. This term can then be used to convert the non-dimensional link lengths of a design back to the matching dimensional lengths that are required in order to achieve the set workspace size.

2.3.4 | Encoder sensitivity

The encoder sensitivity refers to the magnitude of the effect of a small angle displacement at the encoders on the XY position of the end effector. Due to the nonlinear nature of the 5-bar mechanism, the encoder sensitivity is dependent on the pose, as well the direction of the applied displacement. If small

displacements are considered, the sensitivity can be locally seen as linear, and the same value is found regardless of direction. This can be empirically observed.

The encoder sensitivity can be numerically calculated at each pose in the workspace by adding a small displacement of 1 mrad to one of the motor angles (i.e. θ_1) and running the new motor angles through the forward kinematics function. The displacement at the end effector can be calculated by taking the 2-norm of the difference between the position vectors before and after the displacement. The sensitivity is then calculated as the applied angular displacement divided by the resulting end effector movement.

$$sens = \frac{\Delta\theta}{\Delta p} = \frac{0.001}{\|(x'_p \ y'_p)^\top - (x_p \ y_p)^\top\|} \quad (2.8)$$

An example of an encoder sensitivity plot can be seen in [Figure 2.8](#). The global encoder sensitivity atlas is created using the minimum of the encoder sensitivity calculated for all poses within the workspace. A high value indicates that the encoders are sensitive to the movements at the end effector, resulting in a lower required sensor resolution.

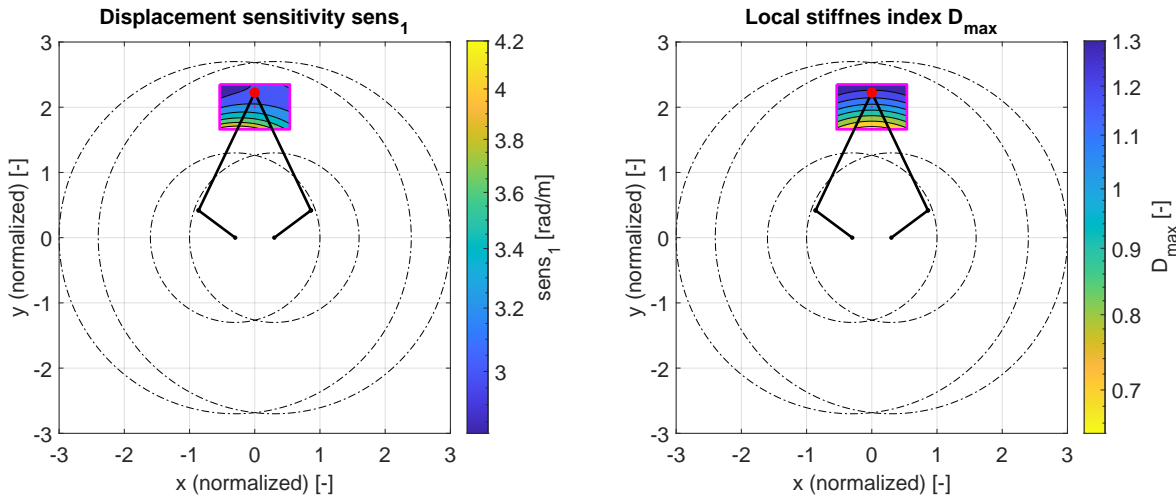


Figure 2.8: Plot of $sens_1$ for a robot in region IVb, plotted only within the workspace. The value of $sens_{1min}$ for this robot is 2.82° . The plot for the other arm is symmetric.

Figure 2.9: Plot of the LSI for a robot in region IVb, plotted only within the workspace. The GSI for this robot is 1.27. Note that the plot is symmetric around the y-axis.

It is important to note that, in order to see the full picture, the non-dimensional sensitivity given by the formula above ($[\text{rad}/-]$) must be brought back to the dimensional world by dividing with the scaling factor. This is especially important when comparing performance regions in the atlas, as the magnitude of scaling needed to reach the desired workspace requirement can drastically influence the sensitivity performance. For example, it might seem like a design has a good encoder sensitivity when looking at the non-dimensional value, but a large scaling factor required to reach the desired workspace would bring down the actual value.

2.3.5 | Stiffness index

The stiffness index is a measure of how the motor stiffness (i.e. controller stiffness) is transmitted through the mechanism to the end effector. To this end, the stiffness matrix K is defined as the ratio between an external force vector τ , applied to the end effector, and the displacement D of the end effector.

$$D = K^{-1}\tau \quad (2.9)$$

In order to calculate the stiffness felt at the end effector, the Jacobian matrix can be used as follows:

$$K = J^\top K_m J \quad (2.10)$$

where the 2×2 diagonal matrix K_m is made up of the two motor stiffnesses on the diagonal. In order to allow for the comparison of kinematic designs at the atlas level, the stiffness values for both motors

are taken as 1. Similarly, the force vector drops out by setting it to a unit force such that $\|\tau\| = 1$. The singular values of the D -matrix represent the maximum and minimum displacements that can be seen at the end effector, by varying the orientation of the force vector. The two values are the lengths of the major and minor axes of the displacement ellipsoid created by the unit force applied to a particular pose of the robot. The displacement values can be calculated from the eigenvalues of the displacement matrix as:

$$\|D_{max}\| = \sqrt{\max(|\lambda_D|)} = \sqrt{\max(|\lambda((K^{-1})^\top K^{-1})|)} \quad (2.11)$$

$$\|D_{min}\| = \sqrt{\min(|\lambda_D|)} = \sqrt{\min(|\lambda((K^{-1})^\top K^{-1})|)} \quad (2.12)$$

In practice, the overall stiffness of the end effector at a given pose is limited by its least stiff direction, which coincides with the largest displacement. Therefore, the $\|D_{max}\|$ value is used as the local stiffness index. In order to maximize the mechanism stiffness, the stiffness index should be minimized. An example of a LSI plot can be seen in [Figure 2.9](#). The global stiffness index is defined as the average of the LSI (similarly to how the GCI is defined).

2.3.6 | Motor torque

While fundamentally not part of the set of kinematic performance indices, the motor torque required to drive the SCARA robot is an important criterion when deciding on the ideal design. This index of dynamical performance is dependent on the acceleration of the robot, as well as its pose (due to the nonlinearity of the kinematics). Because of this pose dependence, the motion of the robot has to be simulated over the poses in a desired trajectory, instead of being calculated up-front.

Dynamic force analysis [18, 19] can be used for this purpose. By applying Newton's second law for the translation and rotation of each link in the mechanism, a set of equations can be used to describe the balance between forces (or moments) acting on each body and the inertial forces (or moments) that result from their change in velocity. Since the motor torques are the only external forces acting on any of the links, the only other forces applied are the joint reaction forces that connect the links together. Due to the assumed ideal hinges at the joints of the mechanism, there are no reaction moments transmitted between links. The inertial forces on each link can be calculated for a prescribed motion profile applied to the end effector. The terms in these equations can be rearranged such that a column matrix x is formed to contain all joint reaction forces and motor torques and a column matrix b , containing the inertial forces and moments. The matrix A can then be made up of the factors used to construct the set of equations as linear combinations of terms in the x and b matrices. The joint reaction forces and the motor torques can then be solved using:

$$x = A^{-1}b \quad (2.13)$$

The motion profile chosen to simulate the torques is a third-order setpoint built to match the specifications in the requirements of the robot, with a maximum velocity of 3 m/s, maximum acceleration of 80 m/s² and a jerk of 4000 m/s³ (required to fit the movement within the required move time), as shown in [Figure 2.10](#). Since the only required movements in the application are straight-line movements along the y-axis, starting from different x-coordinates, all possible movements can be simulated. This allows for the worst case trajectory - leading to the highest torques - to be determined.

The masses and inertias used in the torque calculations are based on a rough estimation of link cross section and zero mass for the joints. As link stiffness is considered during the design phase, the inertias of the various components is likely to increase, leading to the actual required motor torque being higher than calculated here. Still, this torque index is useful as a comparative tool, if not in absolute value.

An example of a torque plot can be seen in [Figure 2.11](#). Note that only the maximum torque for each straight-line movement is plotted over the entirety of the movement's direction. This results in the vertical bands visible in the plot. The global torque index is then defined as the maximum torque required on any of the motors at any point in a straight line trajectory within the workspace. A lower value is beneficial as it implies that weaker motors are required, which minimizes the cost, motor dimensions, heat output etc.

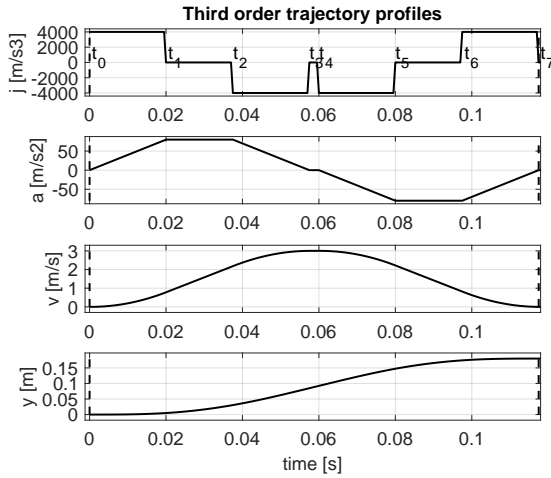


Figure 2.10: Third order setpoint applied to the end effector. The "y" plot represents the displacement in the y direction. There is no change in the x coordinate. Generated using [20].

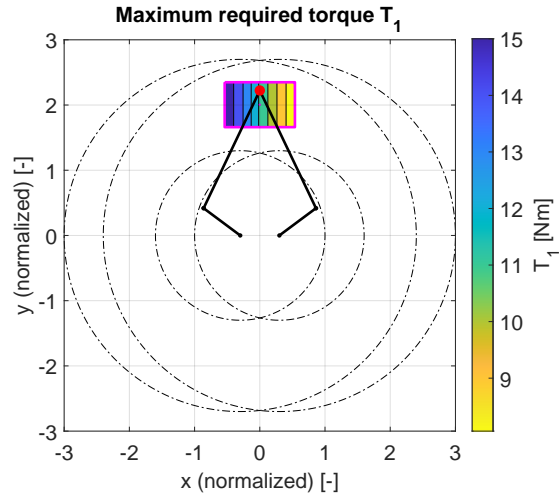


Figure 2.11: Plot of the torque requirement for a robot in region IVb, plotted only within the workspace. The global torque index for this robot is 15.8 Nm. The plot for the other arm is symmetric.

2.4 | Optimum atlas overlap and selection

The performance atlases for the aforementioned indices can be numerically calculated on a discretization of the design space. A 121×121 point grid is used as the discretization of the a- and b-plane, resulting in 5534 valid design points in the trapezoidal design space. The global performance indices of each design are calculated. For this purpose, the non-dimensional workspace is discretized to a grid size of 0.02. The performance atlases are shown in Figure 2.12. The color mapping of each atlas is set such that the best performance is shown in yellow, while the worst is in blue. Some atlases are plotted on a logarithmic scale to better visualize the trends.

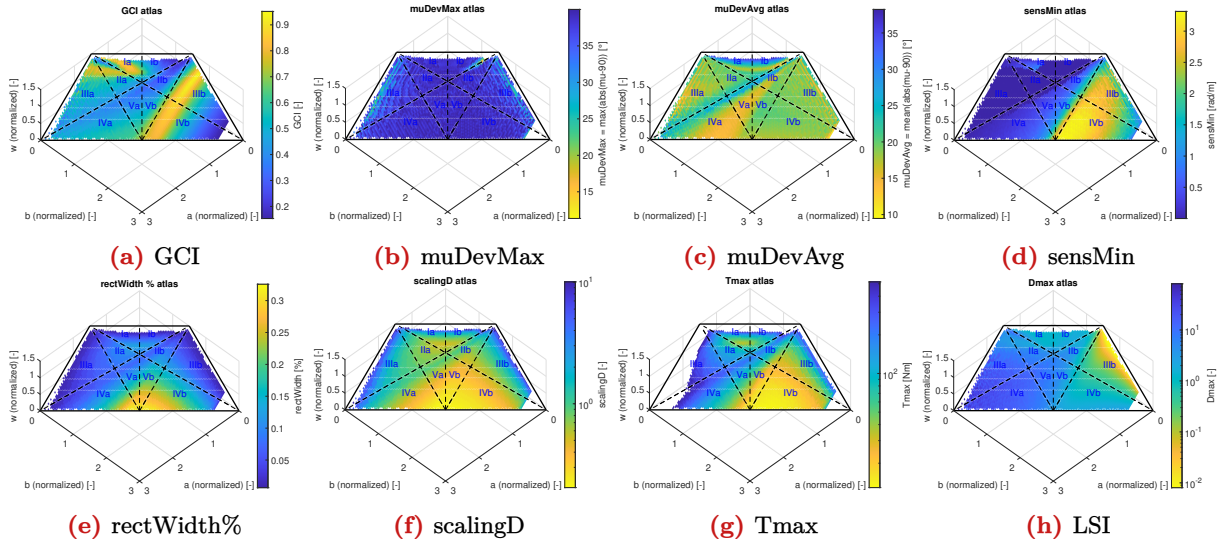


Figure 2.12: Performance atlases. The yellow end of the color bar indicates desired performance.

Several observations can be made based on qualitative inspection of the atlases:

- Missing data points. There are clear regions missing data in all atlases, namely for $b > 2.6$, a or $b < 0.05$ and $w > 1.4$. These are due to the limitations of the workspace discretization size and numerical singularities encountered at the borders of the design space. From the trends visible in the plots, this is not an issue as those regions are not the highly performing ones.
- GCI. A clear band of high-performing designs is visible in the IIIb-IVb regions, indicating the

optimality of $b = 1.7$. A smaller region can also be seen in Ia-IIa.

- muDevMax. This atlas is mostly in the worst end of the spectrum, due to most of the workspace boundaries being defined, at least in part, by the 40° transmission angle deviation limit. This is expected, and a sign of the rectangle finding process working properly.
- muDevAvg. This atlas shows optimality in the IVa-Va regions, with the muDev average being in the order of 10° . Regions IIIb-IVb and IIIa are also decently valued, being around 20° or less.
- sensMin. Encoder sensitivity is found to be highest in the IIIb-IVb regions. Looking at the values encountered, it can be concluded that encoder resolution can be decreased by one order of magnitude by choosing a design in the appropriate region.
- rectWidth% and scalingD. The rectWidth atlas shows the intrinsic spatial inefficiency of picking a workspace limited to within the boundaries of singularities. The percentage of space actively used is upper bound at 30%. The scalingD atlas shows the same information. It is interesting to note that best values for scaling of the workspace and spatial efficiency are found on the axis of $w = 0$, with moderate selections for a and b , in the range of (1, 2).
- Tmax. The best torque performance can be found in the entirety of region IVb. Regions IIb and Vb are not much worse, but also include parts that have worse performance. Choosing a design in the IVb region can result in a ten-fold decrease in the required torque, compared to another reasonable region, and a hundred-fold decrease compared to a bad-performing region.
- Dmax. The stiffness index shows a region of optimality on the edge of IIIb. This converges towards $a = 0$, but naturally, a robot with that small of a driven link would not be feasible. Regions IVb, IIb, Ia and Ib exhibit decent motor stiffness, albeit one or two orders of magnitude worse than IIIb.

The overlap of the performance atlases can also be plotted, as shown in Figure 2.13. The muDevMax was not included as it does not include any useful information. The scalingD atlas was dropped in favor of the rectWidth % one, due to it having a more meaningful numerical value. The relative weights of each index can be used to determine the acceptable percentage of deviation from the best values of each atlas. The atlas values are normalized to the maximum of each atlas. Boundary lines are plotted for the selected regions of each atlas to help with identification. Note that an outlier removal step was taken before plotting the boundaries. Still, sparse outlier data points affect the clarity of some of the boundaries. Moreover, an artificial limit of $b > 1.3$ was applied on the data, in order to avoid the boundaries extending into the left part of the atlas. The same visualization can be applied to $b < 3$, but no meaningful overlap can be observed.

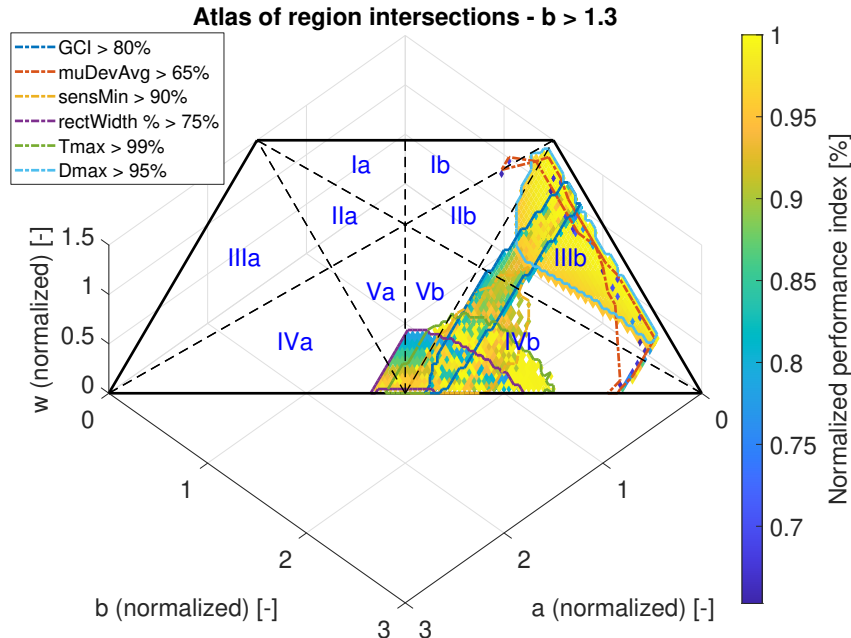


Figure 2.13: Atlas overlap. The percentage below the best value that is permitted for each index is shown in the legend.

If a strict weighing of the different performance indices were to be stated, then an optimal point in the design space could be selected based on the overlap. This is not the case in the current work; instead, multiple candidates can be selected for the optimal design, based on the prioritization of different indices. Most atlases show optimal performance in the IVb region, so selecting a design there would be a reasonable choice. Length Set 1 (LS1) is a middle of the road selection of a design in IVb. That being said, some atlases (mainly the stiffness index) shows optimal behavior in IIIb. LS2 is picked in IIIb, such that the trade-off between the two regions can be analyzed. Since $w = 0$ appears to be the convergence line of several atlases, a design in IVb that has $w = 0$ should also be considered. LS3 is picked for this purpose. For the sake of comparison, LS4 is picked to have the same link length ratios as the original concept that Nobleo considered for the client's application. Note that the resulting dimensional link lengths are not the same as Nobleo's concept, due to the rectangle finding algorithm's constraint on the transmission angle deviation. This results in a robot with links that are ~17% longer. The exact specifications of all length sets can be seen in [Table 2.1](#). The plots of the local performance indices over the workspace of each length set can be found in [Appendix A](#).

Table 2.1: Length set parameters and their global performance indices. A, B and W are the dimensional link lengths, scaled such that the required workspace dimensions are met. WorkspaceDistY is the distance on the y-axis between the origin and the start of the workspace. Clearly good or bad extremes of the parameters are indicated by highlighting in green or red, respectively. The ideal values are specified in the last column.

Parameter	Unit	LS1	LS2	LS3	LS4	Ideal
a	-	0.95	0.35	1.3	1.36	-
b	-	1.7	1.7	1.7	1.36	-
w	-	0.35	0.95	0	0.28	-
A	mm	289.3	335.0	272.2	337.1	-
B	mm	517.7	1627.1	355.9	337.1	-
W	mm	106.6	909.3	0	70.2	-
workspaceDistY	mm	409.1	1257.1	281.2	288.9	0
GCI	-	0.83	0.91	0.79	0.62	1
muDevMax	°	37.99	38.46	38.90	39.25	0
muDevAvg	°	19.42	20.20	16.77	19.50	0
sensMin	rad/m	3.14	2.96	3.27	1.57	∞
sensAvg	rad/m	3.57	3.12	3.72	2.63	∞
GlobalDmax	-	1.16	0.11	2.28	3.37	0
Tmax	Nm	17.20	40.33	13.86	23.55	0

From the quantitative overview in [Table 2.1](#), some takeaways become immediately clear regarding the length sets. LS2, while it has the best GCI and by far the highest stiffness, would result in impractically long links. The required dynamical performance would not be achievable for a link of 1.6 m in length. This can also be observed from the increased torque index. The poor dynamical performance can be linked back to the low rectangle width, which results in a disproportionate scaling factor required to meet the workspace requirements. This design is therefore dropped, but the value of the rectangle width % as an indicator of dynamical performance is noted. The design with $w = 0$, LS3, proves to have the best values for most of the performance indices, including the highest encoder sensitivity and the lowest required torque. LS1 also shows good performance, but LS3 is better across the board. As long as the co-axial motors are not an issue from the design or space utilization perspectives, there is no reason to go for LS1 over LS3. LS4, the original concept that Nobleo considered, has link lengths that are not far from LS1 and LS3. Still, the performance is worse on all metrics considered. This highlights the value of the current method for selecting the optimal design.

From this (mostly) kinematic analysis, it is concluded that the optimal design for a 5-bar SCARA robot, under the aforementioned assumptions and requirements, is one with co-axial motors; a so-called degenerate SCARA [21]. The link lengths to be used in the design phase of this project will be those included in LS3.

3 | Conceptual Design

3.1 | Requirements

Table 3.1 includes the requirements set by Nobleo for the design of the 5-bar SCARA robot manipulator. The requirements are set in such a way that the resulting robot would be functionally equivalent to the manipulator implemented in Nobleo's design.

Table 3.1: Design requirements

Req	Description	Value	Unit
1	Work area	400×256	mm
2	Accuracy of end effector (x,y)	± 50	µm
3	No rotation of end effector	0.1	°
4	Stiffness at end effector	1e6	N/m
5	Picker mass	0.2	kg
6	Picker volume	ø40 x 100	mm
7	Picker stick-out below arm	50	mm
8	Move time (180mm)	120	ms
9	Achievable acceleration	>80	m/s ²
10	Achievable velocity	>3	m/s
11	First eigenmode	>200	Hz

Req3 specifies the maximum rotation around the vertical axis for the end effector. Specifying this is important, as by default the end effector of a SCARA robot does not maintain its orientation (heading) during movements. An element of the design has to ensure the coupling between the fixed world and the end effector rotation. Req5-6 define the design volume and mass of the picker that has to be integrated into the end effector of the robot. Req7 specifies the length of the picker that shall not be enveloped by the components of the SCARA robot. This can be seen as a clearance required around the picker. Req8 defines the move time that must be achieved over the reference movements of 180 mm (as seen in Figure 3.1). These movements start from the back edge of the workspace and are aligned with the y-axis of the planar coordinate system. Req9-10 are derived from Req8 and are the end effector acceleration and velocity that must be achievable in order to meet the move time specification.

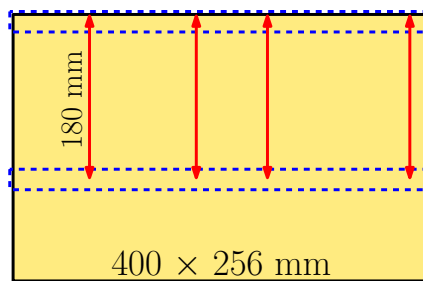


Figure 3.1: Schematic representation of the workspace requirement (Req1), with the approximate pick and place regions shown in blue. The red arrows indicate functional movements from the operation of the robot, in accordance with Req8.

3.1.1 | On the required accuracy and dynamics

The original intention for the move time requirement (Req8) was for it to include any settling time that might be required for oscillations in the position of the end effector to be attenuated, such that the accuracy requirement (Req2) is met. This, however, is dependent on the control performance (stiffness) that can be achieved by the mechatronic system, which only partially depends on its mechanical properties.

Since this is difficult to model formally, a static approach is chosen instead: the ± 50 µm accuracy must be achieved once the movement is over and any residual dynamics have dissipated. This results in a requirement for the accuracy of the encoders, the static stiffness of the arms, as well as any uncertainties in the joints and links. That being said, since there is no motion when the stiffness is to be evaluated, no

forces are applied in the XY-plane to cause any deformations. This leaves only the effects of gravity on the position of the end effector, in the form of sag. This leads to a second-order effect on the XY-position (the first-order effect on the Z position is not relevant as there is no stringent requirement for accuracy in that direction). Furthermore, since gravity is a constant, predictable, external load on the system, the errors induced by it can be calibrated out.

The rationale presented above results in there being no stiffness requirement derived from the fundamental accuracy requirement (Req2). Still, Req4 states an artificial requirement on the stiffness at the end effector (based on forces developed by the picker). The entire accuracy allowance can therefore be attributed to the repeatability (calibrated accuracy) of the encoders, plus, optionally, any asynchronous errors that cannot be calibrated out, such as bearing run-out or thermal effects. Finally, Req11 specifies a lower bound for the eigenmodes of the robot, thus prescribing a minimum level of dynamic performance.

3.2 | Functional breakdown

The functional requirements derived from the aforementioned technical specifications are listed below. The main focus of the functional decomposition was to isolate the design of the joints from that of the links. Since the double SCARA architecture is prescribed, most of the functions are pre-assigned to the components or sub-assemblies that can accomplish them. The function list is ordered starting from the fixed world and going towards the end effector.

1. **Torque supply** - Provide torque to the shoulder joint side of the driven links in order to actuate the manipulator.
2. **End effector position sensing** - Accurately measure the position of the end effector, without interfering with its range of motion.
3. **Motor link stiffness** - Provide a stable and accurate base frame for the robot, with minimal losses to its stiffness. Due to the coaxial motor design chosen in LS3, this function loses much of its substance and is therefore merged with the following one.
4. **Shoulder joint connection** - Provide an axially and radially stiff connection of the driven links to the fixed world, while allowing for torque transmission from the torque supply without introducing play or friction.
5. **Driven link stiffness & mass** - Rigidly connect the shoulder joint to the elbow joint.
6. **Elbow joint connection** - Provide an axially and radially stiff connection between the driven and floating links, without introducing play or friction.
7. **Floating link stiffness & mass** - Rigidly connect the elbow joint to the wrist joint.
8. **Wrist joint connection** - Provide a stiff connection between the two floating links, ensuring the correct number of degrees of freedom is constrained and without introducing play or friction.
9. **End effector volume integration** - Provides the required design volume for the end effector and ensures a rigid connection to the wrist joint.
10. **End effector rotation coupling** - Provides a means of coupling the rotation of the end effector to the fixed world in order to avoid any changes of the picker's heading.
11. **Cables** - Provides sufficient space to route any cables/hoses that must reach the picker.

Each function is further discussed and solutions are proposed and compared. The order in which they are presented is the one that most logically flows from their implementation. This means that, with the exception of a couple of more architectural functions, development starts at the end effector and flows back towards the fixed world.

3.2.1 | End effector position sensing

Typically, the position of the end effector in a SCARA robot is determined in a non-collocated way, by applying the forward kinematics function on the angles measured at the shoulder joints. The precision of this measurement is limited by the stiffness of the links and joints of the robot. Still, any other approach for directly measuring the position of the end effector without limiting its range of motion would

prove impractical and/or inaccurate. This results in the non-collocated method of measurement being implemented, using rotary encoders mounted on the motor shaft.

The repeatability requirement can be numerically evaluated from the encoder sensitivity index. Since no other error sources are taken into account, the entire $\pm 50 \mu\text{m}$ error allowance is attributed to the encoders, resulting in a repeatability of $176 \mu\text{rad}$ that must be achievable at the worst-case pose. This is shown by the "Max encoder disp." graph of [Figure A.3](#), which plots the maximum displacement that can be seen at the end effector for a particular encoder repeatability. This results in the following requirements:

- At least 100° of range. This is easily met, as all rotary encoders of this class offer full 360° rotation.
- Repeatability better than $176 \mu\text{rad}$. This is equivalent to 36 arcsec , 0.01° , $35,120$ counts, or 15.1 bits. Note that the last two values are calculated for a full 360° range. If only a range of 100° is considered, an effective requirement of $9,756$ counts or 13.3 bits would be found.
- Permissible velocity of at least 80 RPM . This is derived from the end effector velocity of 3 m/s .

An absolute angle encoder is preferred over an incremental one, in order for no homing sequence to be required for the identification of the end effector position and ease of implementation. The AksIm-2 [22] line of magnetic encoders from RLS is able to satisfy these requirements, while at a reasonable price (250€ for a 17 bit model). The encoders are available in a variety of sizes and digital communication protocols. Higher resolution (and repeatability) models in the AksIm-2 series are also available. Selecting a better encoder would allow for part of the $\pm 50 \mu\text{m}$ error allowance to be taken up by un-modeled error sources.

3.2.2 | Torque supply

Torque must be provided to the driven links by some sort of electric actuator. While linear actuators could be used to drive the rotational shoulder joints of a SCARA robot, through a lever link [21], this defeats the point of having rotational joints in the first place and adds to the mechanical complexity of the design. Instead, a rotational motor with sufficiently high torque, sometimes referred to as a torque motor, can be used. Due to the high accelerations required, coupled with the large distance between the centers of gravity of the links and the points of application of the force, a torque requirement in the range of multiple tens of Nm is expected (as indicated by the torque index). The non-collocated position measurements result in a series connection of the controller stiffness and the mechanical stiffness of the mechanism connecting the torque supply to the end effector, resulting in the effective actuator stiffness. Since a high actuator stiffness and low play must be achieved, integrating a gearbox of any kind would be detrimental. BLDC (Brush-less Direct Current) motors can be used for this application, as their high torque capacity allows for no further output reduction to be needed. The QTR [23] and QTL [24] series from Tecnotion are in-runner BLDC torque motors with continuous torque ratings of up to 142 Nm . Equivalent motors are also available from other suppliers.

Since the inertias to be driven are not accurately known up-front, the approach taken is to assume that a motor with enough torque is always available, and going up a size of motor is always possible. As the workspace is 281 mm away from the shoulder joint axis, a motor with a diameter of up to 500 mm could easily be integrated in the design. The added mass of a larger motor is not an issue due to the double SCARA topology, with both motors being fixed at the base of the robot. This further reinforces the assumption and allows for the required motor to be determined at the end of the design process.

3.2.3 | End effector rotation coupling

A mechanism must be included in the design, specifically to maintain the orientation of the end effector. This function is truly independent of the ones around it. Potential solutions include either mechanical linking to the fixed world or an active compensation mechanism integrated into the end effector:

- Belt system acting as a virtual 4-bar mechanism, linking the end effector to the base of the robot via one of the arms.
- Linkage system, similar to the aforementioned belt system
- Active compensation actuator capable of sufficient rotation around the vertical axis (R_z) to negate the movement of the end effector.

Due to limited time, the further development of this function was omitted. Still, all possible solutions have the requirement for free rotation of the picker with respect to the wrist joint in common. This aspect is considered in the design and is accomplished by attaching the picker to a set of bearings.

3.2.4 | End effector volume integration

The problem of end effector volume integration summarizes to "how can the $\phi 40 \times 100$ mm design volume of the picker be attached to the wrist joint?". Three topological possibilities emerge:

- 1. Coaxial picker** - The picker volume is integrated within the volume of the wrist rotation axis, as shown in [Figure 3.2a](#). This means that the two bearings required to allow for the rotation of the picker must have an ID of at least 45-50 mm (to also account for the thickness of the interface body). Since the two rotation axes are coincident, this forces the wrist bearings to also be of similar size. From a kinematics standpoint, this is the most elegant choice, also resulting in good dynamics with minimal out-of-plane loads applied on the wrist. That being said, the effect of the mass of four large-diameter bearings and the housing that goes around them might result in worse dynamics overall and more torque required.
- 2. Offset picker** - The picker is offset in front or to the side of the main wrist axis, as seen in [Figure 3.2b](#). This offset would affect the dynamic loads applied by the picker onto the wrist but, at the same time, it allows for the separation of the two rotation axes. This can result in smaller-sized bearings being an option, thus reducing the overall mass of the robot.
- 3. Stacked picker** - The picker is placed below the wrist joint. This allows for vertical separation of the two rotation axes and would permit smaller diameter bearings. This concept is shown in [Figure 3.2c](#). The disadvantage is the increase in the vertical profile of the robot, resulting in out-of-plane dynamical loads and a larger sensitivity (displacement in the XY-plane) to sag. By increasing the stick-out l from the plane of the links, displacement in the XY-plane caused by a wrist sag of z increases linearly (formula approximated from the shortening effect of a leaf spring from [16]):

$$\Delta_{xy} = \frac{(0.5z + l)z}{L} \quad (3.1)$$

where L is the equivalent length of the extended robot arms.

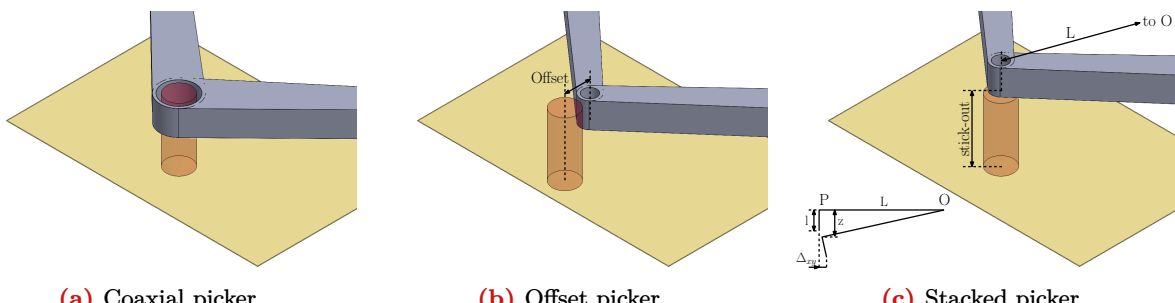


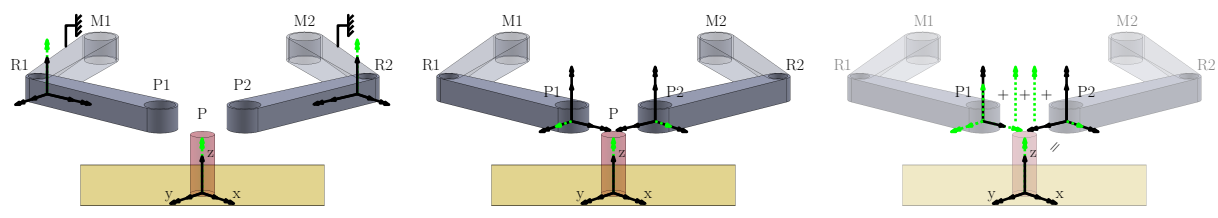
Figure 3.2: Representations of the three picker topology concepts. The picker volume is depicted in red and the workspace area is shown in yellow.

This initial analysis positions the stacked picker as an overall worse version of the offset picker concept, from the bearing size perspective. The first two solutions must be further analyzed in the context of the design of the wrist joint. This is covered in the discussion of the next function.

3.2.5 | Wrist joint connection

The wrist joint must ensure that the end effector can be precisely positioned in space and that the picker is exactly constrained with respect to the fixed world. As mentioned in [subsubsection 3.2.3](#), in order for the picker to be free to rotate in R_z , a set of bearings is added at its interface with the wrist joint. Therefore, the position of the picker must be constrained in 5 degrees of freedom, leaving the rotation around the vertical axis free. Since the two arms of the SCARA robot connect at the wrist in order to constrain it, an analysis of the degrees of freedom must be considered.

Initially, all links are considered to be perfectly rigid beams and the connection at the wrist is broken. The driven links are connected by bearings at the shoulder joints, allowing only for rotation in Rz. This rotation is then constrained by the motors, resulting in all 6 DoFs of the driven links being constrained. The elbow joints similarly constrain 5 DoFs of the floating links by means of a bearing pair, leaving the Rz rotation free, as shown in [Figure 3.3a](#). If the DoFs of the floating arms are considered at the wrist-end, instead of the elbow-end of the links, the free rotational DoF behaves like a translational DoF instead ([Figure 3.3b](#)). If the floating links are directly connected at the wrist joint, it would result in a mechanism with $5 + 5 = 10$ constrained DoFs. If the bearing set that connects the two links together (to allow for relative rotation between poses) and the bearing set that allows for the rotation of the picker are considered, two overconstraints in Rz are removed. In order to alleviate the remaining overconstraints of the wrist, 3 more DoFs must be released, namely Tz, Rx and Ry. This can be achieved either in the wrist joint itself, in one of the links or even split between the two links. For the sake of simplicity, the release of all overconstrained DoFs is assumed to be realized in one of the links, as shown in [Figure 3.3c](#). The R1 - P1 link is now referred to as the *positioning link*, while the other floating link is referred to as the *load link* since it carries most of the load following the introduction of flexibility in the positioning link.



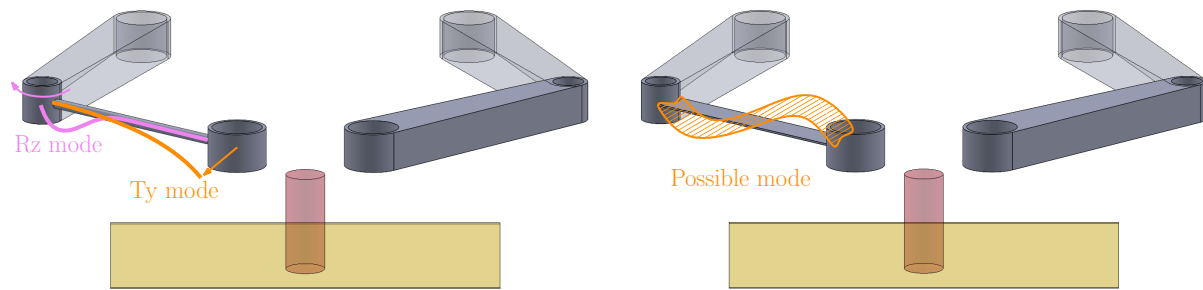
(a) DoFs of the rigid floating arms, observed at the elbow joints. Note that the driven arms are considered fixed by the motors in all sketches. **(b)** DoFs of the rigid floating arms, observed at the wrist joint. The free rotational DoF becomes a translational one. **(c)** DoF calculation considering the flexibility of the positioning arm. The free Rz rotations from the wrist bearings are added.

Figure 3.3: Wrist degrees of freedom. Exploded front-top view: P1, P2 and P are all coincident and form the wrist. Constrained DoFs are depicted by black arrows. Free DoFs are indicated by green dashed arrows. The DoFs depicted at the picker represent the desired exact constraint result. The axis labels from the picker can be used for the other bodies as well.

The positioning arm must only relieve the overconstraints in Tz, Rx and Ry. If a strut were to be used for this purpose, internal degrees of freedom would be introduced in Rz and Ty (by not constraining the existing DoF from [Figure 3.3b](#)). That is because the positioning link side of the elbow bearings, together with the end of the strut positioning link and any mass in between, would be free to move in Rz, only limited by the low hinging stiffness in one of the strut's free directions. This would result in an undesirable low frequency eigenmode significantly below the specified 200 Hz, as depicted in [Figure 3.4a](#). A similar situation is depicted for the Ty mode, which would include the rigid body displacement of the load arm.

The required free DoFs, Tz, Rx and Ry, are much better suited for a leaf spring, as they perfectly match the DoFs that such a flexure releases. By avoiding the introduction of internal DoFs, the eigenmodes of the mechanism would be higher in frequency. This is aided by the rigid directions of the other links being aligned with the flexible directions of the leaf spring (which is a direct consequence of the exactly constrained design). This concept is depicted in [Figure 3.4b](#), where it can also be seen that the possible modes do not include the rigid body displacement of the other bodies. A reinforced leaf spring is even better suited for this, as its axial stiffness, resistance to buckling and internal eigenmodes are increased [16]. The design is further discussed in the relevant function ([subsubsection 3.2.6](#)).

As mentioned, an alternative could be to have both floating arms rigid, and to release the overconstrained DoFs at the wrist joint. This could be achieved by the use of a self-aligning bearing for the wrist connection, which would allow for tilt misalignment between its inner and outer rings. This would release the overconstraint in Rx and Ry. A sliding fit on the bearing shaft or housing could be used to allow for vertical miss-alignment of the links, thus releasing the overconstraint in Tz. The downside of this elegant approach is that commercially available self-aligning bearings have a positive internal clearance [25] which would introduce play in the system, resulting in end effector positioning inaccuracy. A flexural equivalent for a the self-aligning function could be realized (three struts arranged in-plane), but its stiffness is likely to be limited due to the space constraints to allow for integration into the wrist.



(a) Strut design for the positioning link. Examples of possible internal modes due to the internal DoFs are sketched on top. **(b)** Leaf spring design for the positioning link. An example of a higher order internal mode is sketched on top.

Figure 3.4: Possible designs for the flexible positioning link. Note that the exploded view is still used for clarity of the figure; the 3 elements joining at the wrist are in fact coincident.

Regarding the actual connection between the two floating links, several functional requirements are observed:

- Constrains 5 DoFs, leaving Rz free.
- Limited rotation required, in the range of 100°.
- The load link is likely thicker than the positioning link.

These requirements all point toward a symmetric fork design for the hinge, which has the advantage of in-plane force transfer, leading to a lower stiffness loss. Two angular contact bearings in an O-configuration are mounted in the lobes of the fork hinge (adjusted mounting, as described in [25]). This design choice is further discussed in [subsubsection 3.2.7](#), since the elbow has similar requirements.

Returning to the two possible topologies from [subsubsection 3.2.4](#), three concepts are considered for the design of the wrist as a whole. The main differences stem from the combination or isolation of the two rotation axes present at the wrist joint: the one connecting the two floating arms together, and the one connecting the picker to the wrist.

1. **Coaxial picker** - This concept (shown in [Figure 3.5a](#)) combines the two rotation axes and uses an interface sleeve that envelopes the picker volume as the shaft for all four bearings (ID: 50 mm, OD = 72 mm). A 0.5 mm clearance between the OD of the picker volume and the ID of the sleeve ensures that no stresses from the bearings are introduced into the sides of the picker. The picker is connected to the top flange of the sleeve (①).

Axially oversized bushings (②) are included between bearings in order to achieve the required (form-closed) preload. This leads to complications during the assembly of the robot which are hereafter referred to as *in situ press fit*. The transition fit of the bearing housings and shafts (as described in [subsubsection 3.2.10](#)) requires the use of a press for mounting. The difficulty is caused by having to bring both floating arms into alignment before inserting the interface sleeve from the top bearing bore. Moreover, the oversized bushings would have to also be positioned at the same time. While theoretically possible, with the required tooling and jigs, this is impractical from an assembly standpoint.

In order to preload the four bearings, a preload ring is bolted onto the sleeve from the bottom. The 4.5 mm wall thickness of the sleeve provides limited space for bolts to go into (③).

2. **Offset-fixed picker** - This concept separates the two rotation axes, allowing for the use of smaller bearings for the connection between the floating links, as seen in [Figure 3.5b](#). A sleeve is still used for the mounting of the picker, however both the sleeve and the picker bearings are smaller in diameter: 45 mm ID bearings and 2.5 mm wall thickness for the sleeve.

The connection between the load and positioning links is done at an offset from the picker axis. The bearings have the positioning link as the housing. A shaft (①) is inserted into the bearings and bolted to the wrist joint body. The assembly of this shaft would also suffer from the *in situ press fit* issue. This could be avoided by making provisions for the shaft to first be press fitted into the

positioning link and only then for that arm to be brought into alignment with the wrist joint itself. This would require a large opening in the side of the wrist joint and would decrease the stiffness of the joint, but it would alleviate the issue.

3. Offset-pivoting picker - This concept, depicted in [Figure 3.5c](#), returns to the coincident rotation axes of the coaxial picker concept, however without the integration of the picker within the axes. This allows for the use of small diameter bearings across the board, reducing the mass of the joint drastically. An intermediary shaft ((1)) acts as the shaft for all four bearings. The shaft connects to the picker via its exposed top and bottom ends. The rotation of the picker would then be a pivoting motion around the wrist joint.

This concept suffers from the same in situ press fit issues as the coaxial picker, just at a smaller diameter. The reduced size of the shaft also complicates the attachment of the preloading rings, as surface area for bolting ((2)) is limited.

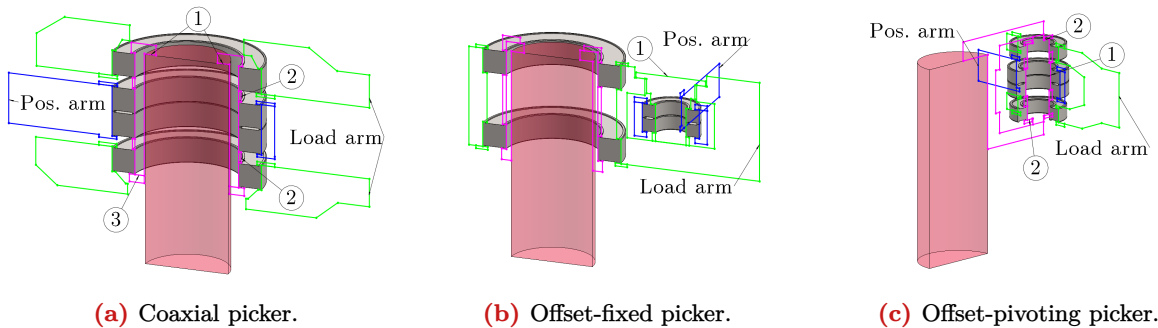


Figure 3.5: Sketches of the three picker integrations in the context of the wrist joint. Interfaces to the continuations of the floating arms are indicated. The structure connecting the picker to the wrist joint is colored magenta.

Following this comparison, concept 2 is chosen as it should have decent mass and dynamic behavior, while not suffering from the bolt space issue and the in situ press fit situation can be avoided.

It is important to note that the offset location of the picker, caused by the design of the wrist joint body, is not included in the initial kinematic calculations from [section 2](#). Due to this offset, the workspace covered by the picker will be different from that covered by the wrist joint axis. This implies that the global performance of the design will not exactly match with the values calculated previously. Still, since the offset is relatively small, the effect on the optimality of the link length choice is considered negligible.

3.2.6 | Floating link stiffness & mass

The main functional requirement for the floating links is to rigidly connect the wrist to the elbow joints. The design of a link can be split into independent sub-components:

- A structural beam element, and
- Two joint interfaces to attach the link to the joints.

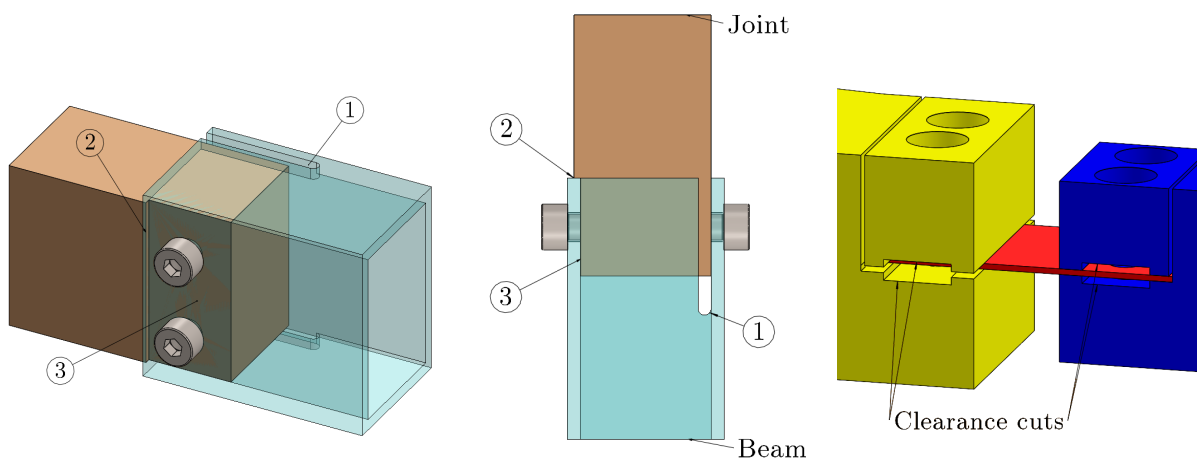
Looking at the beam element, several options are possible to rigidly connect the two joint interfaces. Since the design must have good stiffness and dynamic performance, the optimal choice would be a hollow beam [[16](#)]. The load on the floating links is mostly bending due to gravity, as well as axial compression and tensile stresses due to in-plane dynamic loading. This means that a rectangular cross section with a large height and reduced width would be appropriate. Three options are possible for the construction of this hollow rectangular beam, assuming the material used to be aluminium:

1. **Extruded boxtube** - readily available in various sizes and with various wall thicknesses.
2. **Plate construction** - Constructing a boxtube out of plates (for example, by welding of castellated laser cut plates) offers an increased flexibility compared the commercially available boxtubes. This includes finer control over the sizes and wall thickness, but also allows for a (non-linearly) varying cross section over the length of the beam. This can result in a more optimal stress distribution and a lower mass overall. Furthermore, plate construction would facilitate the creation of hollow beams out of more exotic materials, not usually available in boxtube form (i.e. carbon fiber composites).

3. Milled billet - Milling the bulk of a solid piece of stock material can be used to reach a hollow cross section, however care has to be taken to close off the opened face used to access the milled region. This is to ensure a closed box design, which is critical for resistance to torsion [16].

The boxtube option strikes a good balance between design flexibility, cost and complexity and is the chosen option.

Regarding the joint interface, several aspects must be considered. First of all, the beam must connect to a protrusion from the joint bodies and it is preferred that the mating surfaces would have easy access for bolting. This results in a design where the beam envelops the joint protrusion, as opposed to the converse. Moreover, the mating surfaces should be precise and allow for the exactly constrained attachment of the boxtube. The concept proposed is shown in [Figure 3.6a](#) and [Figure 3.6b](#). The flexibility cuts (①) on one side of the boxtube allow for the two boxtube walls to clamp onto the joint interface without introducing uncertainty into the positioning of the beam. One of the sides (③) of the joint interface is precisely machined to act as a reference surface for the XY alignment of the beam to the joint. Similarly, a reference lip (②) is included to precisely define the overall length of the link. Since the Z alignment is not critical, no reference surface is included for that direction.



(a) Link-joint interface, trimetric view (b) Link-joint interface, top view (c) Leaf spring clamping interface.

Figure 3.6: Sketches of the three picker integrations in the context of the wrist joint. Interfaces to the continuations of the floating arms are indicated. The structure connecting the picker to the wrist joint is colored magenta.

In the case of the positioning floating link, leaf springs are included between the beam and the joints at both ends, forming a reinforced leaf spring flexure. The leaf springs are clamped to the joints and boxtube as shown in [Figure 3.6c](#). The clamping area is minimized by introducing a clearance cutout, in order to avoid virtual play from hysteresis in the clamped joint [16].

3.2.7 | Elbow joint connection

The elbow joint must facilitate the load transfer from the end effector towards the base of the robot, while also constraining the DoFs of the floating link. The following requirements can be stated:

- Constrains 5 DoFs of the floating link, leaving Rz free.
- Limited rotation required, in the range of 90°.
- The load link is likely thicker than the positioning link.

Two hinge topologies are possible: side-by-side or forked, as depicted in [Figure 3.7](#). While the side-by-side design would allow for a simpler design of the joint, the forked hinge is always preferred as it allows for symmetric, in-plane, force transfer, resulting in a stiffer connection overall [16]. It is important to note that the side-by-side design is more permissive to large transmission angle ranges, but that is not something that the chosen link length set requires.

This results in the forked hinge design being chosen. The fork part of the hinge is mounted to the generally larger sized driven link, while the shaft of the hinge is connected to the smaller sized floating link.

In order to facilitate assembly and avoid requiring an in situ press fit of the shaft (hinge pin), the bearing shaft is designed to first be pressed into the bearings on the fork side and then to be attached to the floating link. This avoids the press fit issue and simplifies assembly and handling. In order to ensure alignment, two angled surfaces (forming a V-receptacle) (1) contact the cylindrical surface of the shaft. This design is shown in [Figure 3.8](#). This interface is drawn together by two bolts (2). An alignment pin (3) ensures the Z alignment of the hinge halves and adds stiffness to the interface.

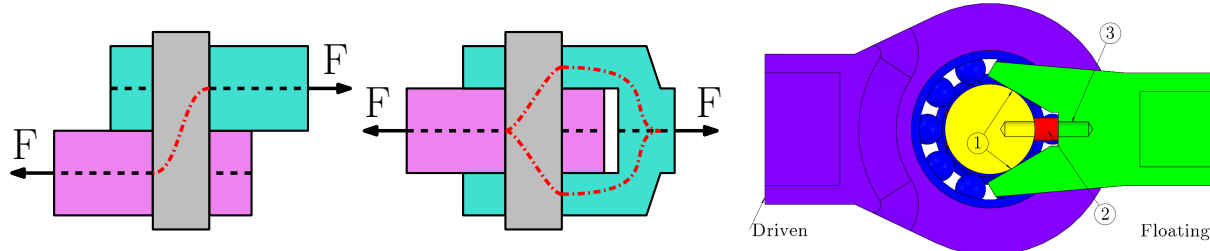


Figure 3.7: Side-by-side (left) vs. forked (right) hinge design (side view). The force path is sketched in red.

Figure 3.8: Top cross section of elbow joint conceptual design.

3.2.8 | Driven link stiffness & mass

The design of the driven links is equivalent to that of the floating links described in [subsubsection 3.2.6](#). The loading of the driven links is however dependent on the pose of the robot. In an extended configuration, when the driven and floating links are almost colinear, the loads on the driven links are similarly oriented to those on the floating links. In a retracted configuration, where the transmission angles are closer to 90°, most of the load transferred at the elbow joint reaches the driven links as torsion. The driven links must therefore also be resistant to torsion. This implies the use of cross sections that are both tall and wide, closer to a square than a rectangle.

3.2.9 | Shoulder joint connection

The complexity of the shoulder joints stems from the coaxial motors design choice. Moreover, since fork-style hinges are used throughout the design, all links are coplanar. This includes the two driven links, which must therefore connect to the shoulder axis in the same point in space. Of course, this is not possible in practice and some axial clearance must be present between the drives for the two links. Several conceptual topologies are considered below. The components are rotationally symmetric around the rotation axis (with the exception of the driven links and the encoder readhead). The entire drive system used to drive one arm is mirrored against the XY-plane of the links in order to drive the second arm. All concepts include the driven link, a set of bearings, a BLDC motor and an encoder, as depicted in [Figure 3.9](#).

Since the radial dimensions of the components in the schematics are roughly in scale, the quality of a concept can be evaluated by how vertical the connecting lines between components are. A line close to vertical implies a straight connection without the need for a large change in the diameter of the connecting structure. Moreover, the lines connecting the fixed world and those connecting the moving world must not intersect. Several possible topologies for the aforementioned components have been considered, the best of which are discussed below and depicted in [Figure 3.9](#):

1. **Natural** - This concept features all components in the positions that they would naturally connect to the shoulder. Since the link comes in radially into the shoulder axis, it is natural for the bearing constraining its motion to have its outer ring moving with the link. This creates the need for a fixed shaft at the center of the shoulder, for the inner ring of the bearing to connect to. The BLDC motors manufactured by Tecnoton are inrunners, meaning that the rotor is on the inside of the stator. This nicely coincides with the moving ring of the bearing above it. Since the moving world must continue down until the encoder, the stator has to be suspended in space by a secondary fixed

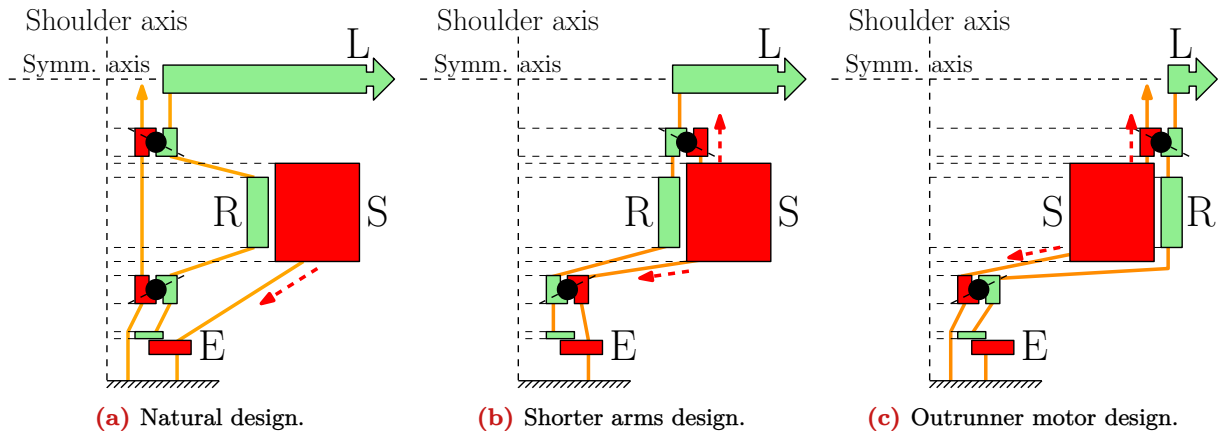


Figure 3.9: Concept sketches of the shoulder joint topologies, including the end of a driven link (L), the bearings, the motor rotor (R) and stator (S) and the encoder (E). Components that are connected to the fixed world are colored red, while components that are connected to the moving links are colored green. Structural connections are depicted by orange lines. Heat conduction from the coils of the motor is indicated by red arrows.

world, instead of connecting to the fixed shaft at the center of the shoulder joint. The connecting lines in this concept can be made more vertical by increasing the size of the bearings.

2. Shorter arms - This concept takes inspiration from the FAMM and increases the overall diameter of the shoulder axis, while reducing the length of the beams that make up the driven links. The kinematic length of the links is still the same, but the shoulder bearings are closer to the elbow joint, resulting in a stiffer construction. This concept also explores the possibility of flipping the orientations of the bearings. By having the inner ring connected to the driven link, the need for a fixed shaft at the core of the shoulder is removed. This would allow for a solid moving shaft to be included, instead of the hollow one described by the previous concept. The possibility of having the diameter of the bearings differ between the two in the pair is also considered. The main disadvantage here is that the bearings are now directly connected to the stator of the BLDC motor. While this is a convenient connection from a topology stand point, it results in significant heat conduction, from the heat-generating coils within the stator, to the bearings. This can have disastrous consequences on the form-closed bearing preload used to ensure the stiffness of the shoulder bearings.

3. Outrunner - This concept explores the benefits of using an outrunner motor instead of an inrunner. Undoubtedly, the topology of this concept is more convenient, with the moving side of the motor aligning with the moving link. That being said, the issue of heat conduction is also present in this concept. Furthermore, the advantage of outrunner motors over inrunner motors is that it is generally easier to extract the heat from the outside surface of an inrunner, than it would be to extract it from the (smaller area) inside surface of an outrunner [26].

Due to the heat conduction effects described above, the first concept has a significant advantage over the others. Having a secondary structure connect the heat-generating stator to the fixed world is a good way of ensuring that the bearing preload will remain constant, instead of degrading over the up-time of the robot. In practice, a combination of the natural and the shorter arms concept is used, such that the diameter of both bearings is more in line with that of the motor. Moreover, the readhead of the encoder will be thermally insulated from the heat coming from the stator, by removing its connection to the fixed world from the path of the dissipated heat.

Concept sketches for all three options were drafted, however no new observations were made, as the topological analysis proved to be sufficient for determining the optimal concept. The design allows for mirroring against the link plane, in order to drive the second arm. The concept sketch for the chosen design is shown in Figure 3.10. The column at the core of the shoulder joints is common for both motors and acts as the shaft for the bearings, which are preloaded by means of a ring (①) that is bolted on at the end of the column. Bolted rings are also used to secure the outer rings of the bearings (②) and the rotor (③) to the moving shaft. Isolation of the bearing preload force from the positioning of the encoder ring must be a design consideration for ring ②. The stator is secured to its mounting cup by another

bolted ring (④).

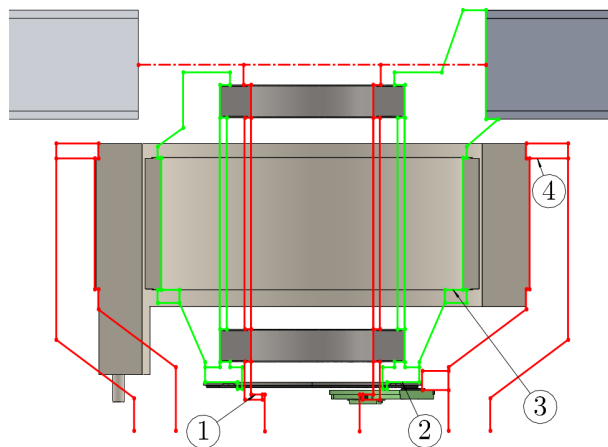


Figure 3.10: Sketch of the natural shoulder joint concept for one motor. Components that are connected to the fixed world are colored red, while components that are connected to the moving links are colored green.

3.2.10 | Bearing selection

This section covers several important concepts regarding bearing selection and application. In order to constrain 5 degrees of freedom for a joint, the choice was made to go for a set of angular contact ball bearings. When properly preloaded against each other, this type of bearing offers stiffness both in radial and axial directions. Typically angular contact ball bearings are mounted in pairs (or multiple pairs) right next to each other and are preloaded by pressing the two bearings together. This results in a bearing arrangement that offers good axial and radial stiffness and locates the shaft axially, but does not offer much tilt stiffness. A secondary bearing is then needed to constrain the radial direction at a different point on the shaft. A cylindrical roller bearing is typically used for this, as shown in [Figure 3.11a](#). Together, the pair of angular contact ball bearings and the cylindrical roller bearing exactly constrain the shaft, while also allowing for thermal expansion of the shaft (the roller bearing does not constrain the shaft axially) [27]. This typical arrangement is not applied in this design. Instead, the two angular contact ball bearings are mounted in a so-called *adjusted arrangement*, where the bearings are spaced out on the shaft and preloaded via the structure of the shaft and housing, as depicted in [Figure 3.11b](#). This allows for the bearing poles to be spaced out further apart. This develops tilt stiffness from the two angular contact ball bearings, without the need for a third radial bearing. The adjusted bearing arrangement can be used on applications with relatively short shafts, where thermal expansion has limited influence on the preload of the system [25].

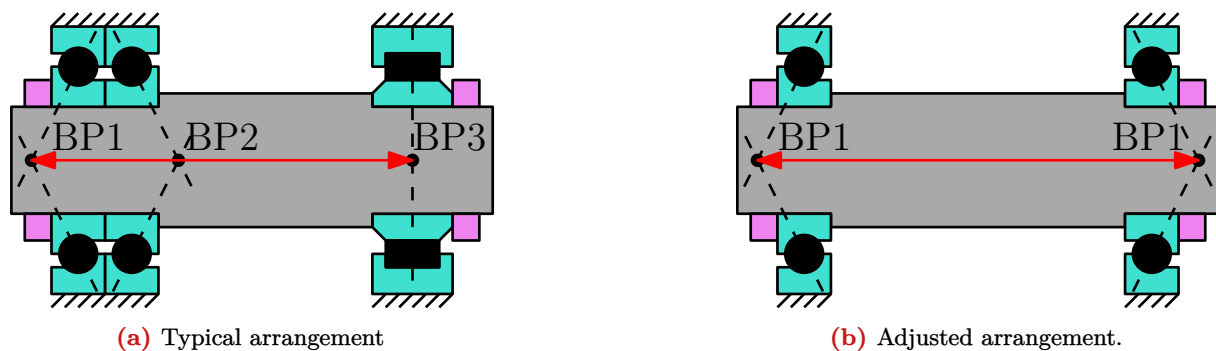


Figure 3.11: Two possible bearing arrangements that employ angular contact ball bearings to constrain a shaft. Lock rings used to preload the bearings against shoulders in the shaft are shown in pink. Bearing poles are indicated by black dots and the bearing pole distance relevant for tilt stiffness is marked by a red arrow.

The preload of the angular contact ball bearing pairs at each joint is achieved by means of pressing them together via axially oversized bushings. This results in a form-closed preload, which is sensitive to thermal expansion. Instead of a form-closed preload, a force-closed design can be considered, where springs are used to apply a virtually constant force to the bearing rings [16]. Still, [27] argues that spring-based preloading is not suitable for applications where high stiffness is required and that form-closed preloading is viable, as long as there is no direct heat input on the shaft.

In order to achieve the required radial location of the bearing rings in their housings, some degree of an interference fit is required when mounting [27]. While a transition fit is sufficient for this purpose, a press would still have to be used when assembling the bearings into the joints. This results in the *in situ press fit* issue mentioned in previous sections.

SKF offers super-precision angular contact ball bearings in four dimensional series, such that multiple outer ring diameters and rolling element diameter are available for the same shaft size. SKF recommends the 718 series for high stiffness applications, such as robotic manipulators [27]. These bearings have the smallest cross section and the smallest rolling elements, resulting in the highest stiffness when preloaded. Due to their small size, the 718 series bearings do not have a sealed variant. Since adding an external seal to each shaft in the robot would add unnecessary complexity, the choice was made to go for the slightly larger 719 series.

3.3 | Design embodiment

The design following from the chosen concepts explained above is detailed using the SOLIDWORKS 2024 CAD package. A top-down approach was chosen, with the dimensions of elements being defined by layout sketches. Furthermore, extensive use of external referencing between the dimensions of components was made, such that changes to dimensions of one component automatically propagate to other connected components. **Figure 3.12** shows a dimetric view of the whole assembly.

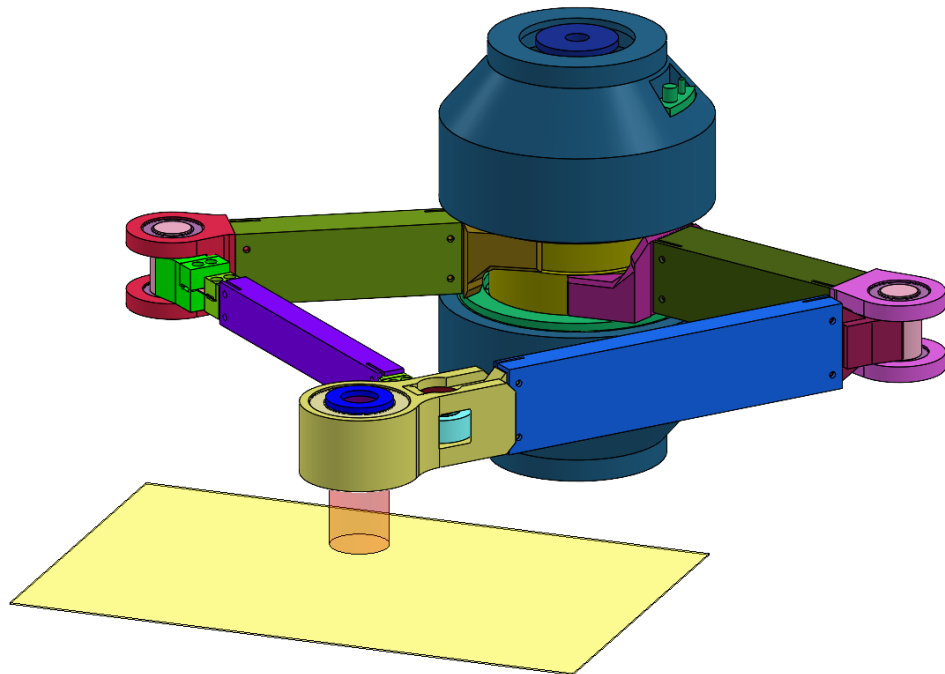


Figure 3.12: Dimetric view of the full robot assembly. The robot's workspace is shown in yellow. The robot is in a centered pose, with the picker in center of the workspace.

The following sections cover the design considerations and relevant dimensions of the components. Note that the current level of maturity of the design did not warrant for the modeling of small components and fixtures such as bolts or bearing preload rings.

3.3.1 | Links

All links are made out of aluminium boxtubes and follow similar designs. The joint interface features 20 mm deep, 2 mm wide, flexibility cuts and a pair of M4 bolt holes on each side, as seen in [Figure 3.13a](#). An overview of the link dimensions can be seen in [Table 3.2](#). The cross sectional dimension are chosen such that the stiffness and eigenfrequency requirements are met, or maximized as much as possible.

Table 3.2: Link dimensions.

Link	Kinematic length [mm]	Boxtube length [mm]	Cross section [mm]	Wall thickness [mm]
floating-positioning	355.9	210.9	20x30	3
floating-load	355.9	257.9	20x60	3
driven-positioning	272.2	152.2	30x50	3
driven-load	272.2	152.2	40x50	3

The floating positioning link depicted in [Figure 3.13a](#) includes two leaf springs and their required adapter blocks. The leaf springs are 40 x 20 x 0.75 mm in size. The translational stiffnesses of the this link are simulated to be:

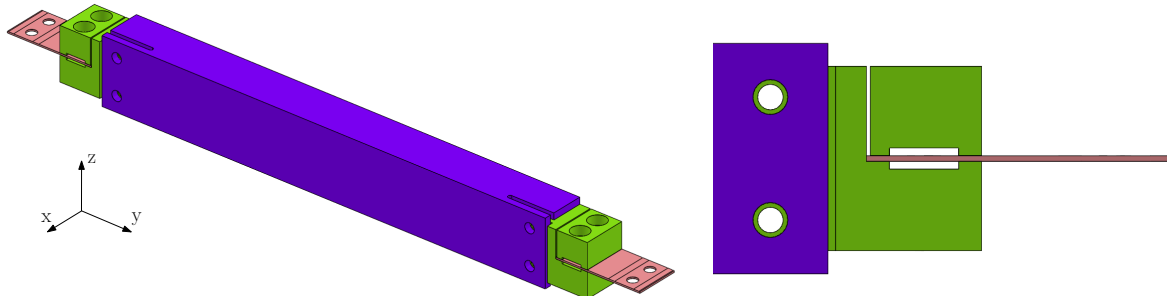
$$c_x = 3.81e7 \text{ N/m}$$

$$c_y = 2.52e4 \text{ N/m}$$

$$c_z = 2.85e2 \text{ N/m}$$

where z is the free direction of the link and the other two are considered rigid (see local coordinate system in [Figure 3.13a](#)). This leads to a stiffness ratio of 88.5, between the desired stiffness and the undesired stiffness. This ratio is below but close to the ratio of 100 at which a flexure is generally considered to be a flexure [28].

The leaf springs are clamped over two areas of 3 mm x 20 mm, as seen in [Figure 3.13b](#). The clamping force is provided by two M4 bolts that thread into the bottom half of the clamp body. This clamping geometry is repeated at all interfaces with the leaf springs.



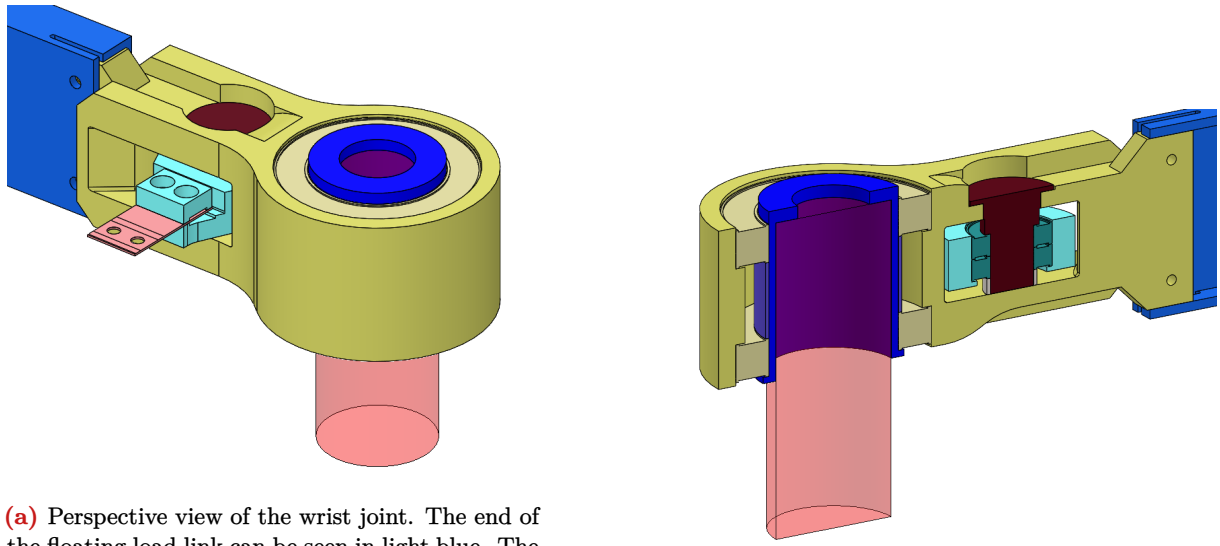
(a) Perspective view of the positioning floating link. The lines visible on the leaf springs are split lines used to properly connect the mating surfaces in FEM.

(b) Side view of the leaf spring (pink) clamping adapter (green) at one end of the positioning floating link.

Figure 3.13: CAD views of the link design.

3.3.2 | Wrist joint

The wrist joint is made up of a monolithic joint body machined out of aluminium that houses the picker bearings and connects the two floating links. The current design can be seen in [Figure 3.14a](#). The bearing arrangement, as well as the stiffening ribs on the top and bottom surfaces can be clearly observed in [Figure 3.14b](#). Two 71909 bearings (ID: 45 mm, OD: 68 mm) are used to support the picker and two 71902 bearings (ID: 15 mm, OD: 28 mm) act as the connection between the two floating links.



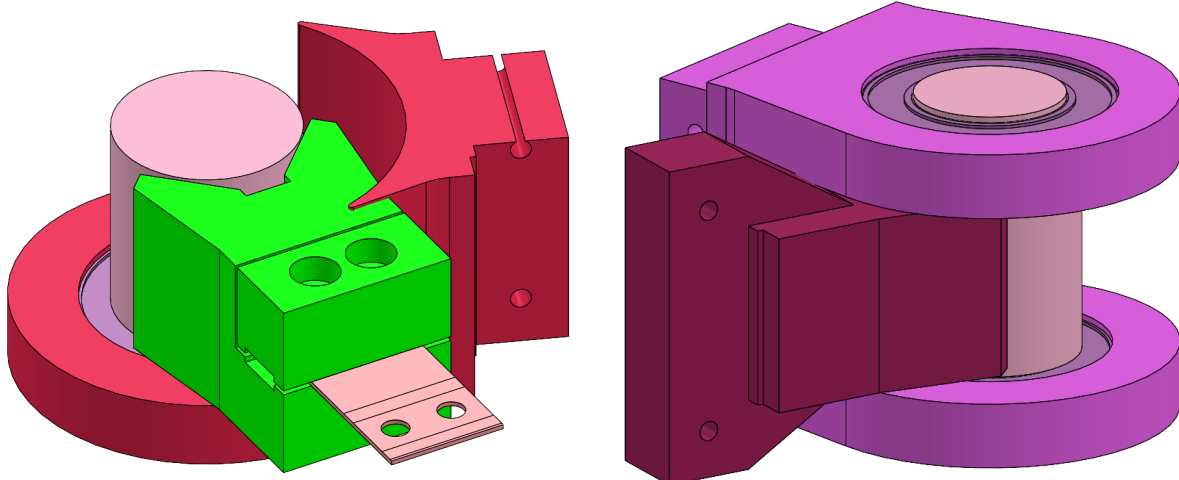
(a) Perspective view of the wrist joint. The end of the floating load link can be seen in light blue. The connection pin for the positioning arm is shown in brown.

(b) Dimetric cross section view of the wrist joint. The picker sleeve can be seen in dark blue.

Figure 3.14: CAD views of the wrist design.

3.3.3 | Elbow joints

The two elbow joints have the same geometry, however the dimensions of the joint interfaces are adapted to meet the inner dimensions of their respective link boxtubes. Both joints feature two 71905 bearings (ID: 25 mm, OD: 42 mm) as part of the fork design. The joint shaft, part of the floating link side of the elbow joint, has an OD of 30 mm. Two M6 bolt holes as well as a 5 mm alignment pin allow for the connection to the joint body. On the positioning side, the floating link elbow joint body includes the required clamping features to attach to the leaf spring. The two elbow joints can be seen in [Figure 3.15](#).



(a) Dimetric section view of the positioning elbow joint. A collision between the fork (red) and the leaf spring interface body (green) can be observed. The V shaped shaft interface can also be observed.

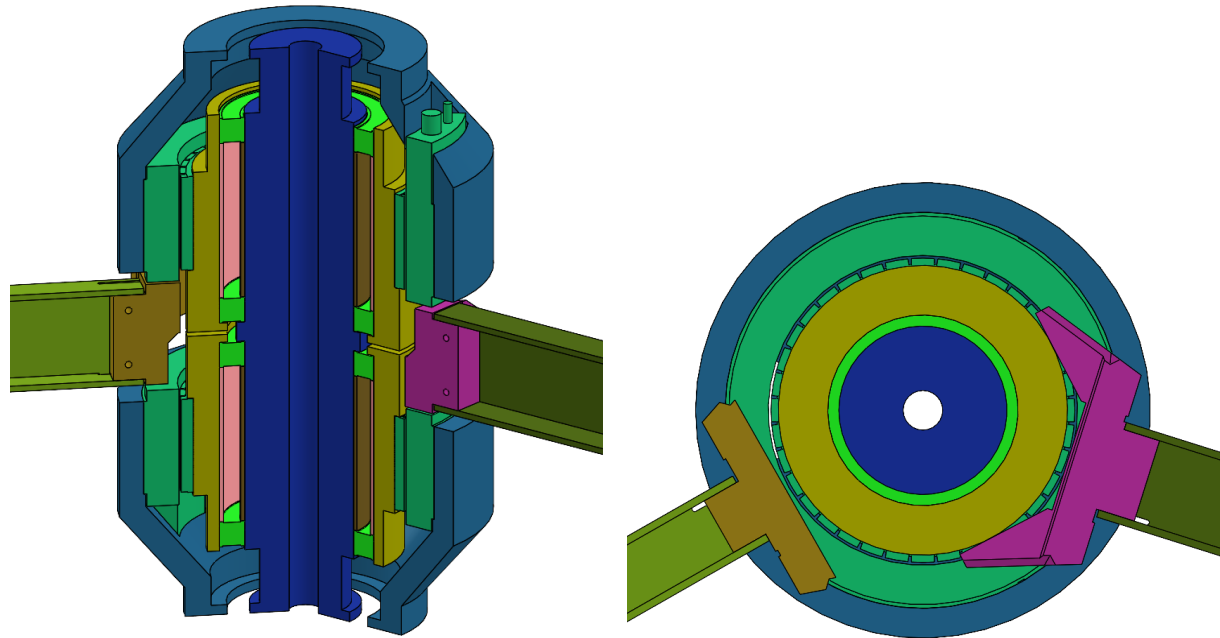
(b) Dimetric view of the load elbow joint. The length reference lip on the boxtube interface (dark red) can be observed.

Figure 3.15: CAD views of the elbow design.

3.3.4 | Shoulder joints

The shoulder joint, shown in [Figure 3.16a](#) is based on a 292 mm long cylindrical column, with the lowest shoulder diameter of 45 mm. Two 71912 bearings (ID: 60 mm, OD: 85 mm) connect to the moving

shoulder shaft. This shaft features the required OD to interface with the rotor of the Tecnotion QTR 160-60 motor. The motor is clamped as per the manufacturer's instructions, using the specified surfaces. A stator cup goes around the moving shaft and rigidly connects the motor stator to the fixed world. The connection from the shoulder shaft to the driven links is not detailed to a high degree (see [Figure 3.16b](#)) and the current model results in collisions between the interfaces when the robot is in an extended pose. The design concept shown for the interface resembles the one used at the elbow joints. The mounting points for the encoders are not modeled, however sufficient volume and clearance is included for them.



(a) Dimetric section view of the shoulder axis, showing the internal components, including the motors (turquoise), the bearings (lime green) and rotating shoulder shafts (dark yellow).

(b) Top section view of the shoulder design, showing the currently non-detailed connection piece (magenta) between the shoulder shaft and the load arm.

Figure 3.16: CAD views of the shoulder design.

3.4 | Evaluation

The performance of the design can now be evaluated by making use of the Computer Aided Engineering features included in the SOLIDWORKS package.

3.4.1 | Modal analysis

The eigenmodes of the entire robot assembly are evaluated using SOLIDWORKS Simulation Frequency studies. The robot is evaluated at multiple poses at the edges of its workspace, in order to find the worst case dynamic performance. The central pose is also evaluated for the sake of comparison. The following list includes assumptions and modeling choices that were made:

- The picker is modeled as a rigid body with the specified mass.
- The leaf springs are modeled using shell elements, while the rest of the model uses solid elements. This allows for the mesh of the leaf springs to be of sufficient quality, while a coarser mesh is used for the larger scale components. This results in a simulation with ~2.5 million DoFs, that can be solved using SOLIDWORKS' iterative solver and fits within 20 GB of RAM. Additional information about the meshing settings and the resulting mesh quality can be found in [subsection B.1](#).
- The motors, stator cups, preload bushings, preload lock rings, bearings and any bolts are not modeled. This includes the mass of the motor rotors, which should be connected to the moving components.

- The shoulder column is connected to the fixed world at its top and bottom surfaces using spring fixtures with $1e15$ N/m stiffness.
- Perfect controller stiffness is simulated by locking the rotation of the rotor mounting surfaces to the fixed world. This is modeled using spring fixtures with $1e15$ N/m stiffness.
- The rotation of the picker is constrained using spring connections between its bearing seats and the wrist body. The springs have $1e15$ N/m shear stiffness.
- All angular contact ball bearings are modeled as rigid bearing connections.
- The bolts used to connect the link boxtubes to joints are modeled as pinned connections, with rotation and translation constrained. This does not perfectly model a bolted connection, but it is a good approximation.
- The leaf springs are connected using bonded interactions between the clamped surfaces.
- No external loads are applied to the model.

The results of the simulations for the centered and front-right poses can be seen in [Figure 3.17](#), in the form of a plot of the first 12 eigenfrequencies of the robot. Note that, due to unknown reasons, the simulation also returned several erroneous modes, which have been manually removed. Still, the rest of the results appear to be valid. More details on the erroneous modes can be found in [subsection B.2](#). [Figure 3.18a](#) shows the first mode of the robot in the centered pose. The mode shape seen in the first mode is the expected one: the elbow of the positioning arm oscillates in the vertical direction, in part due to the flexibility of the leaf springs. It can also be visually observed that the connection between the shoulder shaft and the driven boxtube on the positioning side loses a lot of stiffness in this mode. [Figure 3.18b](#) shows the first mode of the robot in the front-right pose. The first mode in this pose is the same as in the centered pose, also stemming from the flexibility of the positioning arm.

As the lowest mode in the worse pose is at 202 Hz, the eigenfrequency requirement of 200 Hz can be considered met, under the aforementioned assumptions. The design could be further optimized in order to include a safety margin from the 200 Hz requirement.

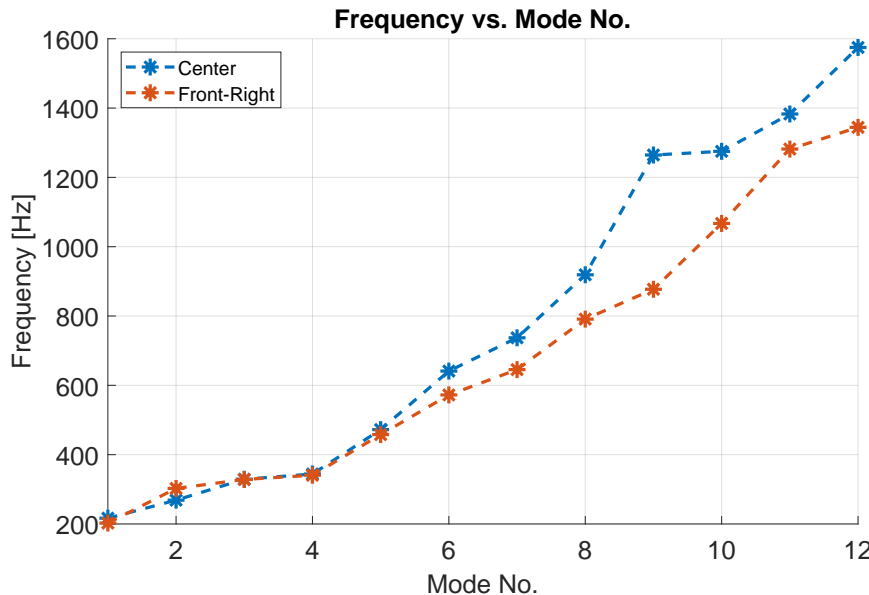


Figure 3.17: Plot of the frequencies of the first 12 eigenmodes. Note that any erroneous modes returned by the simulation have been removed.

The next nine modes in the centered pose can be seen in [Figure 3.19](#). This shows that the second mode is the vertical elbow mode of the load arm. This mode is 50 Hz higher than the first one. Mode 3 is the internal torsion mode of the reinforced leaf spring. Modes 4, 5, 7 and 8 are also higher internal modes of the reinforced leaf spring link. The same modes are also visible in the front-right pose, however the order starts to differ after mode 5. Modes 2-9 for the front-right pose can be found in [Figure B.3](#).

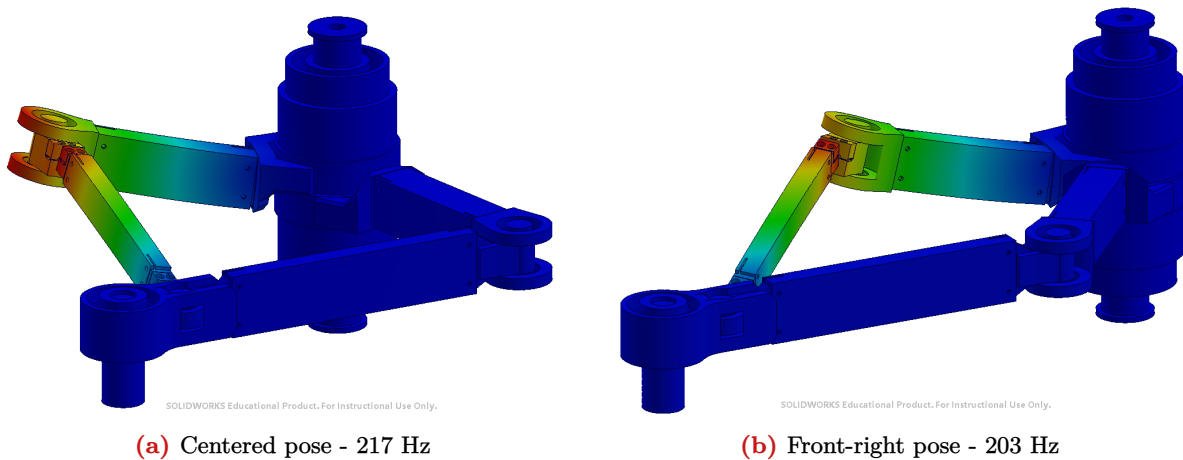


Figure 3.18: Mode 1 for two poses of the robot. The resultant displacement amplitude is plotted over the deformed model.

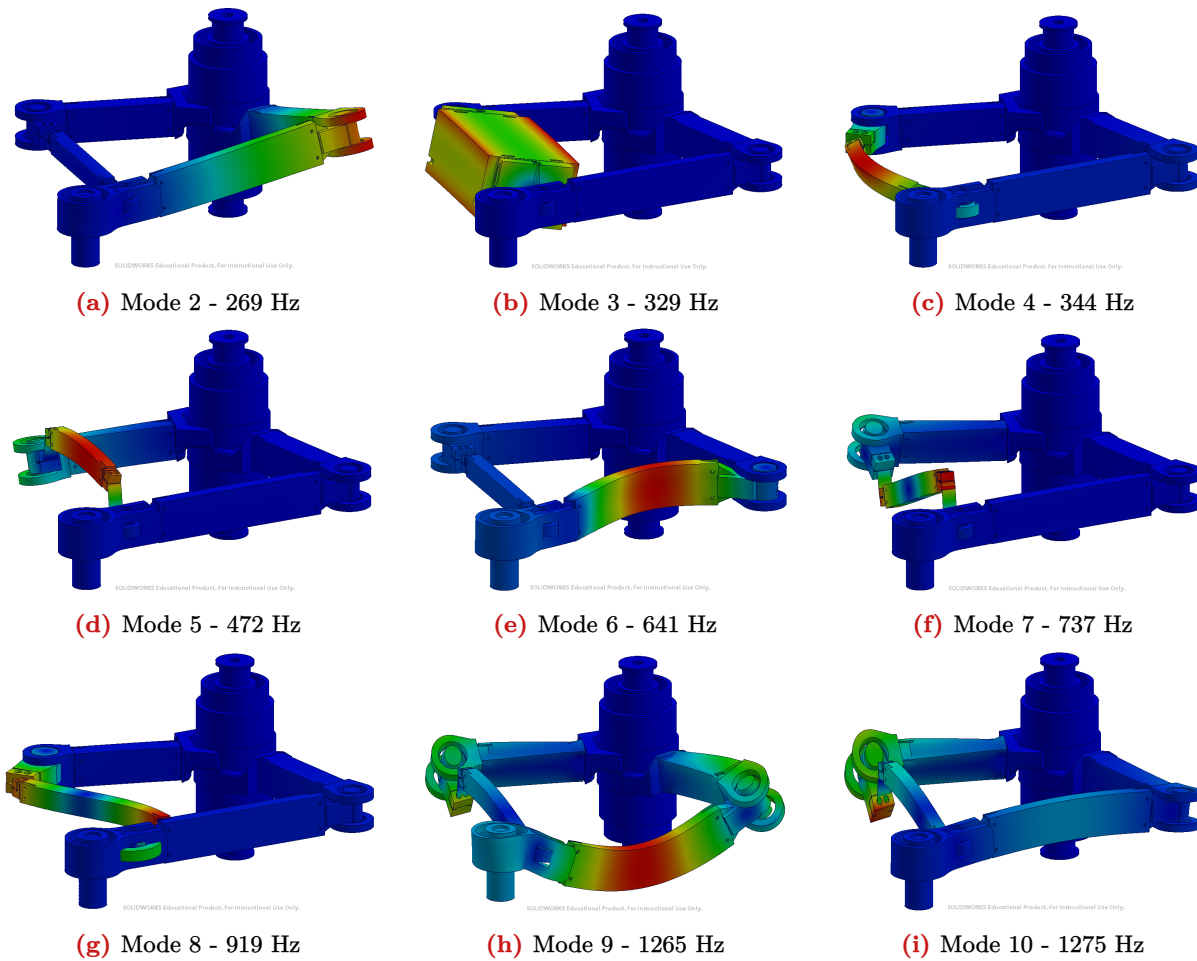


Figure 3.19: Modes 2-10 in the centered pose. The resultant displacement amplitude is plotted over the deformed model.

3.4.2 | End effector stiffness

The stiffness at the end effector is simulated using a SOLIDWORKS Simulation Static study. The assumptions, connections and mesh sizes are the same as in the Frequency study. A 1 N force is applied to the bottom surface of the picker volume. The orientation of the force is changed and the simulation is run for all three directions. The displacement of the end effector is calculated as the average of the displacement in the direction of the applied force, over all nodes on the bottom surface of the picker.

Running the simulations reveals that the vertical direction is the least stiff of the three and therefore the one that defines the overall stiffness of the robot. **Figure 3.20** shows the magnitude of the displacement of the robot caused by the vertical force applied to the picker. The displacement measured in the centered pose is $4.4\text{e-}6$ m, leading to a vertical stiffness of $2.3\text{e}5$ N/m. The displacement measured in the front-right pose is $5.3\text{e-}6$ m, leading to a vertical stiffness of $1.9\text{e}5$ N/m. The lowest of these two stiffnesses is 5 times lower than the required $1\text{e}6$ N/m, meaning that the stiffness requirement is not met by the current robot design.

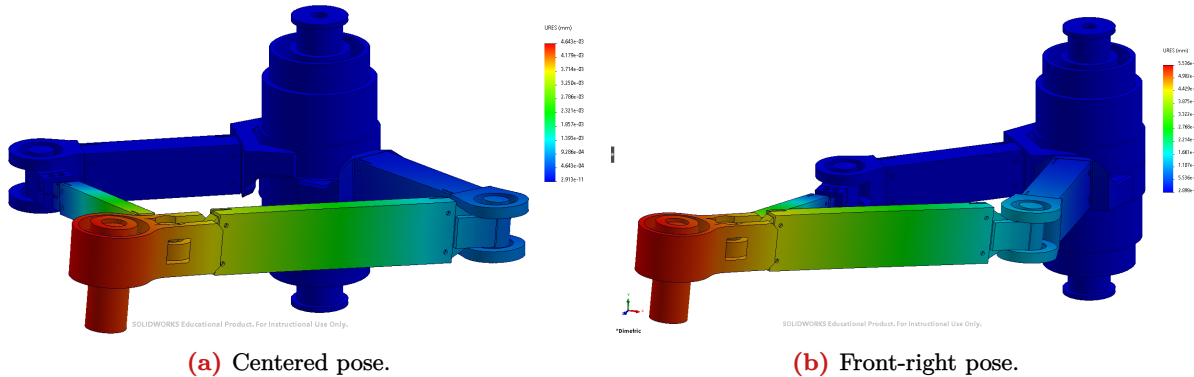


Figure 3.20: Resultant displacement magnitude plots for the two poses considered.

3.4.3 | Motor torque

The motor torques are simulated using a Motion Study enabled by SOLIDWORKS Motion. This feature uses the mates in the top-level assembly to run a multi-body simulation of the assembly's dynamics. In order for this feature to properly function, there must not be any redundant mates in the assembly. This can be avoided by using hinge mates and the careful application of mate primitives where needed. As in the FEM simulations, the motors, stator cups, preload bushings, preload lock rings, bearings and bolts are not included in the study.

Rotary motor features are applied at the rotor interfaces of the shoulder shafts. The motion of these motors is prescribed based on externally loaded data points that have been exported from the MATLAB kinematics study. The motion is simulated for two straight line movements: one along the y-axis, with $x = 0$, and one on the right side of the workspace, along $x = 200$ mm.

Figure 3.21a and **Figure 3.21b** show the torques calculated by SOLIDWORKS Motion. For $x = 0$, both motors must develop torques that are almost equal, as expected. The small difference in magnitude can be explained by the different boxtube cross sections and the offset picker. The magnitude of the maximum torque required is 38 Nm. When $x = 200$ mm, the expected asymmetric behavior can be observed. One motor has to develop upward of 53 Nm, while the other motor only has to develop 13 Nm. The motor that has to develop the largest torque is the one connected to the arm on the side of which the movement is performed. A similar torque value is expected to be encountered on the left side of the workspace.

Taking a small safety margin, the required torque in order to satisfy the specified motion profile would be at least 60 Nm for each motor. This is outside the continuous torque range of the QTR 160-60 that is currently modeled in this design. Since higher design height options are not available in the QTR 160 series, a jump to the QTL 210 model is required. This series of motors has a 210 mm outer diameter, thus requiring larger shafts to connect to, resulting in more inertia. The smallest motor in the QTL range, the QTL 210-65 is capable of developing 65 Nm of continuous torque which satisfies the requirement and is likely to also cover the increased inertia due to the motor size increase.

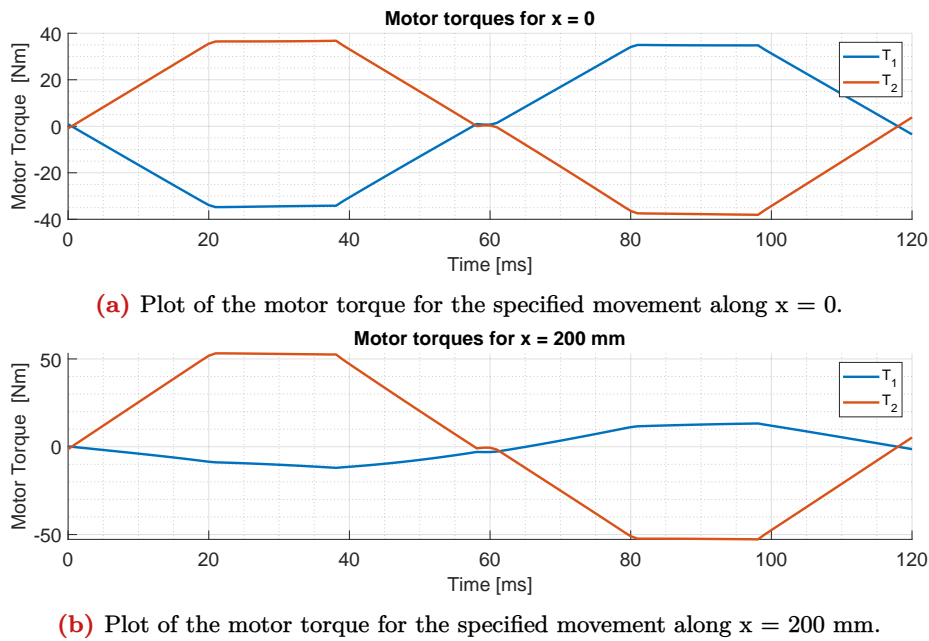


Figure 3.21: Motor torque plots over two different movements aligned with the y-axis.

4 | Conclusion

The present work covers the first steps of the design of a double SCARA robot manipulator, from a set of requirements, to a conceptual design embodiment of the optimal robot. A set of link lengths is determined by means of a study of the kinematic performance of all possible robot topologies. The requirements set for the robot were then converted into functional requirements which were developed independently and then integrated into a viable robot concept. The resulting conceptual design was evaluated using several finite element and motion simulations.

The kinematic analysis based on the overlap of performance atlases proved to be a very effective way of determining the optimal kinematic design for the 5-bar mechanism. Through this method, it could be concluded that, at least for the current set of kinematic requirements, the optimal robot design is one co-axial shoulder joints and floating links ~30% longer than the driven links. The fact that dynamic performance indices, such as the torque index, could be integrated into the workflow speaks to the versatility of the approach. Finally, the fact that the entire infinite design space can be condensed to a 2D plane, leading to the performance of all possible designs being plotted in one figure is truly remarkable.

The functional requirements for the SCARA robot are determined and a conceptual embodiment of their solutions is realized in CAD. A light and stiff design was selected for the links, in the form of hollow aluminium boxtubes with different cross sections, depending on the loads applied onto them. Pairs of adjusted angular contact ball bearings are used at every joint in order to properly constrain the degrees of freedom of the links. Forked hinge designs are used where possible, so that the bearing tilt stiffness is maximized and the force path is kept in-plane. The exact constraint of the picker is achieved by relieving all overconstraint DoFs through a reinforced leaf spring integrated into one of the floating links. The driven links are actuated by a pair of BLDC inrunner motors, the coils of which are thermally isolated from the joint bearings, allowing for a constant preload force.

Most of the technical requirements listed in Table 3.1 are successfully met by the proposed conceptual design, with the exception of the stiffness requirement. The achieved value of $1.9e5$ N/m is 5 times lower than the required $1e6$ N/m. This, however, does not necessarily indicate the infeasibility of the concept as further improvements of the detailed mechanical design can be applied, including the redesign of several components. A motor torque of 60 Nm is determined to be necessary for the robot to be able to follow the desired motion profile. This results in rather large motors being required, however the topological advantage of the double SCARA design results in their high mass and diameter not being an issue.

5 | Recommendations

The present work should be continued, leading to the eventual realization of a prototype. Multiple aspects of the approach taken can be improved. The following list includes several directions that continuing this work could follow:

- **Detailing of the mechanical design**, such that the requirements are met and all components are properly modeled, to the point where a prototype can be constructed. Redesign of several components, including the wrist joint body, which currently features a large through-hole to accommodate the floating link of the positioning arm, as well as the interfaces between the driven links and the shoulder joints.
- **Further improvements to the kinematic analysis** by including new performance indices.
- **Expanded robot synthesis process** that could include the semi-automated design of mechanical components. This could be used to quickly develop and evaluate the feasibility of this robot concept for a variety of applications.
- **Validation of FEA results.** The results obtained from the SOLIDWORKS FEA package include unexplained behavior that has been knowingly ignored. While the validity of the claims in this work is still trusted, further research into the sources of these errors should be done.
- **Further study into existing SCARA robot concepts** including, but not limited to, the FAMM robot. It is important to note the similarities between the optimal kinematic design concept proposed in this work and that of the FAMM.
- **Evaluation of the validity of assumptions**, such as the ones regarding the chosen working mode or of the location of the largest inscribed rectangles in the workspace.
- **Traversing singularities.** An exploration into the possible optimality of robot designs that make use of a workspace distributed over multiple singularity regions should be undertaken.

References

1. Makino, H. Development of the SCARA. *Journal of Robotics and Mechatronics* **26**, 5–8. doi:[10.20965/jrm.2014.p0005](https://doi.org/10.20965/jrm.2014.p0005) (Jan. 2014).
2. Fyler, D. C. *CONTROL ARM ASSEMBLY US Pat. 4,712,971*
3. Gamble, B. J. *5-Bar Linkage Kinematic Solver and Simulator* tech. rep. (University of Vermont, Apr. 2020). <https://scholarworks.uvm.edu/hcoltheses/406>.
4. Theingi, Li, C., Chen, I.-M. & Angeles, J. *Singularity Management Of 2DOF Planar Manipulator Using Coupled Kinematics* in *Seventh International Conference on Control, Automation, Robotics And Vision (ICARCVOZ)* (2002), 402–407.
5. Liu, X.-J., Wang, J. & Pritschow, G. Kinematics, singularity and workspace of planar 5R symmetrical parallel mechanisms. *Mechanism and Machine Theory* **41**, 145–169. doi:[10.1016/j.mechmachtheory.2005.05.004](https://doi.org/10.1016/j.mechmachtheory.2005.05.004) (Feb. 2006).
6. Huang, M. Z. Design of a Planar Parallel Robot for Optimal Workspace and Dexterity. *International Journal of Advanced Robotic Systems* **8**, 176–183. doi:[10.5772/45693](https://doi.org/10.5772/45693) (2011).
7. Choi, J.-H., Lee, C., Kim, M.-E. & Lee, J. *Singularity Analysis of a 5-bar Planar Parallel Mechanism Based on a Geometric Measures* in *IEEE International Symposium on Robotics (ISR) 2013* (IEEE, Oct. 2013).
8. Demjen, T. *et al.* Design of the five-bar linkage with singularity-free workspace. *Robotica* **41**, 3361–3379. doi:[10.1017/S0263574723001042](https://doi.org/10.1017/S0263574723001042) (Nov. 2023).
9. Liu, X.-J., Wang, J. & Pritschow, G. Performance atlases and optimum design of planar 5R symmetrical parallel mechanisms. *Mechanism and Machine Theory* **41**, 119–144. doi:[10.1016/j.mechmachtheory.2005.05.003](https://doi.org/10.1016/j.mechmachtheory.2005.05.003) (Feb. 2006).
10. Feng, G., Zhang, X.-Q., Zhao, Y.-S. & Hong-Rui, W. A Physical Model Of The Solution Space And The Atlas Of The Reachable Workspace For 2-DOF Parallel Planar. *Mechanism and Machine Theory* **31**, 173–184 (1996).
11. Steenbakkers, M. H. A. *Evaluation and improvement of the FAMMDD: Notch- and Gain scheduling for a fast and accurate manipulator* tech. rep. (Technische Universiteit Eindhoven, 1997). <https://research.tue.nl/en/studentTheses/evaluation-and-improvement-of-the-fammdd>.
12. Schipper, D. A. *Mobile Autonomous Robot Twente* PhD thesis (Universiteit Twente, Enschede, 2001). <https://research.utwente.nl/en/publications/mobile-autonomous-robot-twente-a-mechatronics-design-approach>.
13. De Boej, J. *Getting the FAMM-DD operational* tech. rep. (Technische Universiteit Eindhoven, Jan. 2002). <https://research.tue.nl/en/publications/getting-the-famm-dd-operational>.
14. Van Helvoort, J. J. M. *Analytical and experimental LFT modeling of a double scara robot* tech. rep. (Technische Universiteit Eindhoven, Nov. 2003). <https://research.tue.nl/en/studentTheses/analytical-and-experimental-lft-modeling-of-a-double-scara-robot>.
15. Verstraeten, D. C. C. *Simulation and software development of the FAMM* tech. rep. (Technische Universiteit Eindhoven, Jan. 2003). <https://research.tue.nl/en/publications/simulation-and-software-development-of-the-famm>.
16. Soemers, H. *Design Principles for Precision Mechanisms* (University of Twente, 2011).
17. Wikipedia. *Ternary search* https://en.wikipedia.org/wiki/Ternary_search. Date accessed: 22/11/2024
18. Willamst, R. J. & Rupprecht, S. Dynamic Force Analysis of Planar Mechanisms. *Mechanism and Machine Theory* **16**, 425–440 (1981).
19. Dynamic Force Analysis. *Chapter 2: Dynamic Force Analysis Lecture Notes on Dynamics of Machinery*
20. Lambrechts, P. *Advanced Setpoint Generation Toolbox*
21. Tempea, I., Neacsu, M. & Livadariu, A. A new acting solution of a double SCARA robot in *The 3rd International Conference on "Computational Mechanics and Virtual Engineering" COMEC 2009* (Oct. 2009), 765–770.
22. RLS. *AksIM-2* <https://www.rls.si/eng/aksim-2-off-axis-rotary-absolute-encoder>. Date accessed: 27/10/2024
23. Tecnotion. *QTR-160 series* <https://www.tecnotion.com/products/qtr-torque-160-series/#gallery-2>. Date accessed: 27/10/2024
24. Tecnotion. *QTL-210 series* <https://www.tecnotion.com/products/qtl-torque-210-series/#gallery-2>. Date accessed: 27/10/2024
25. SKF Group. *Rolling bearings* <https://cdn.skfmediahub.skf.com/api/public/0901d196802809de>. Date accessed: 10/10/2024

26. Tecnotion. *Inrunner vs outrunner Torque motor White Paper* <https://www.tecnotion.com/downloads/inrunner-motor-vs-outrunner-motor/>. Date accessed: 10/11/2024
27. SKF Group. *Super-precision bearings* <https://cdn.skfmediahub.skf.com/api/public/0901d19680495562/>. Date accessed: 12/10/2024
28. Henein, S., Cosandier, F., Rubbert, L. & Richard, M. *Flexure Mechanism Design* (EPFL Press, 2017).

A | Length set local performance plots.

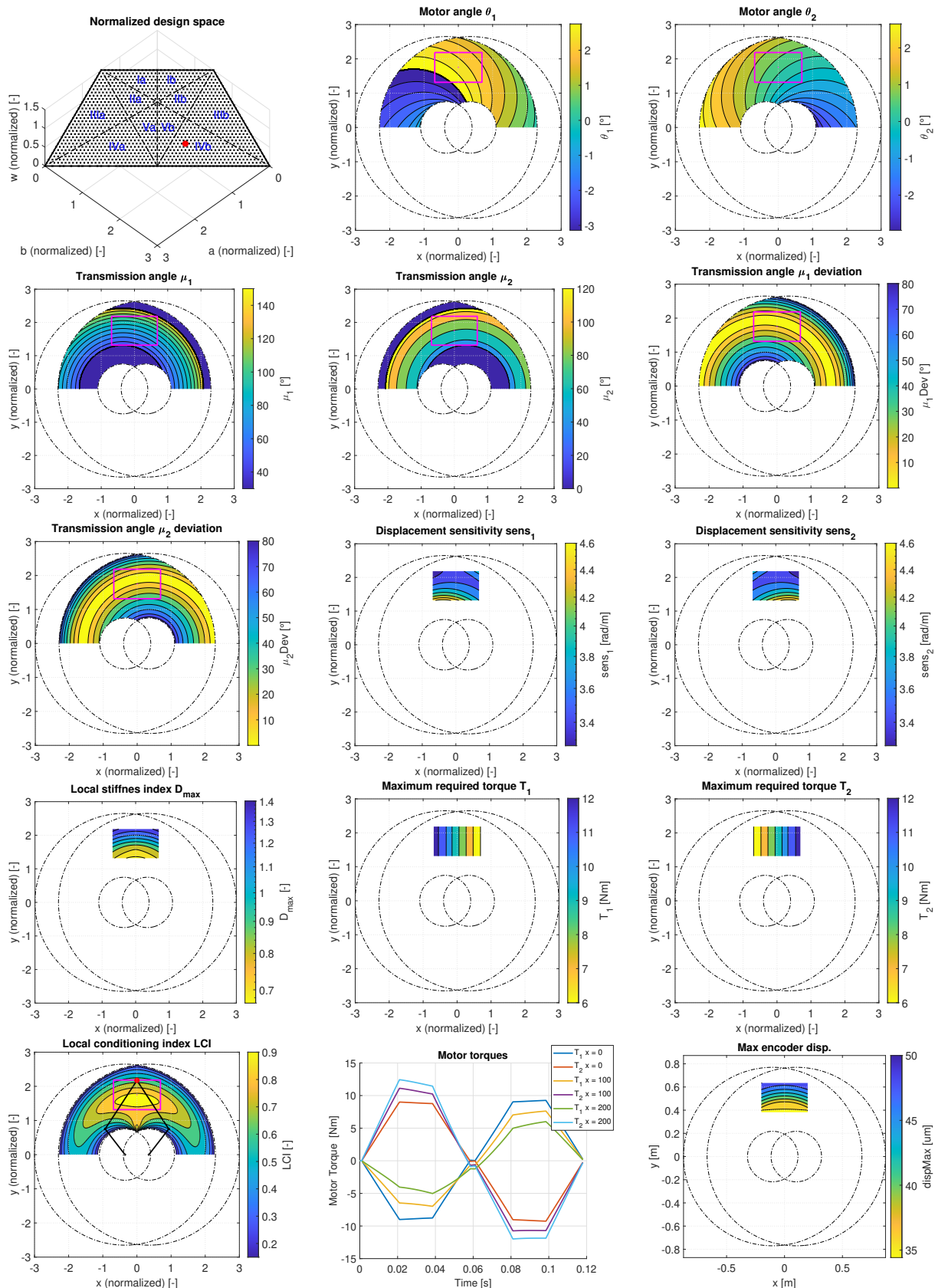


Figure A.1: Local performance indices plotted over the workspace of LS1.

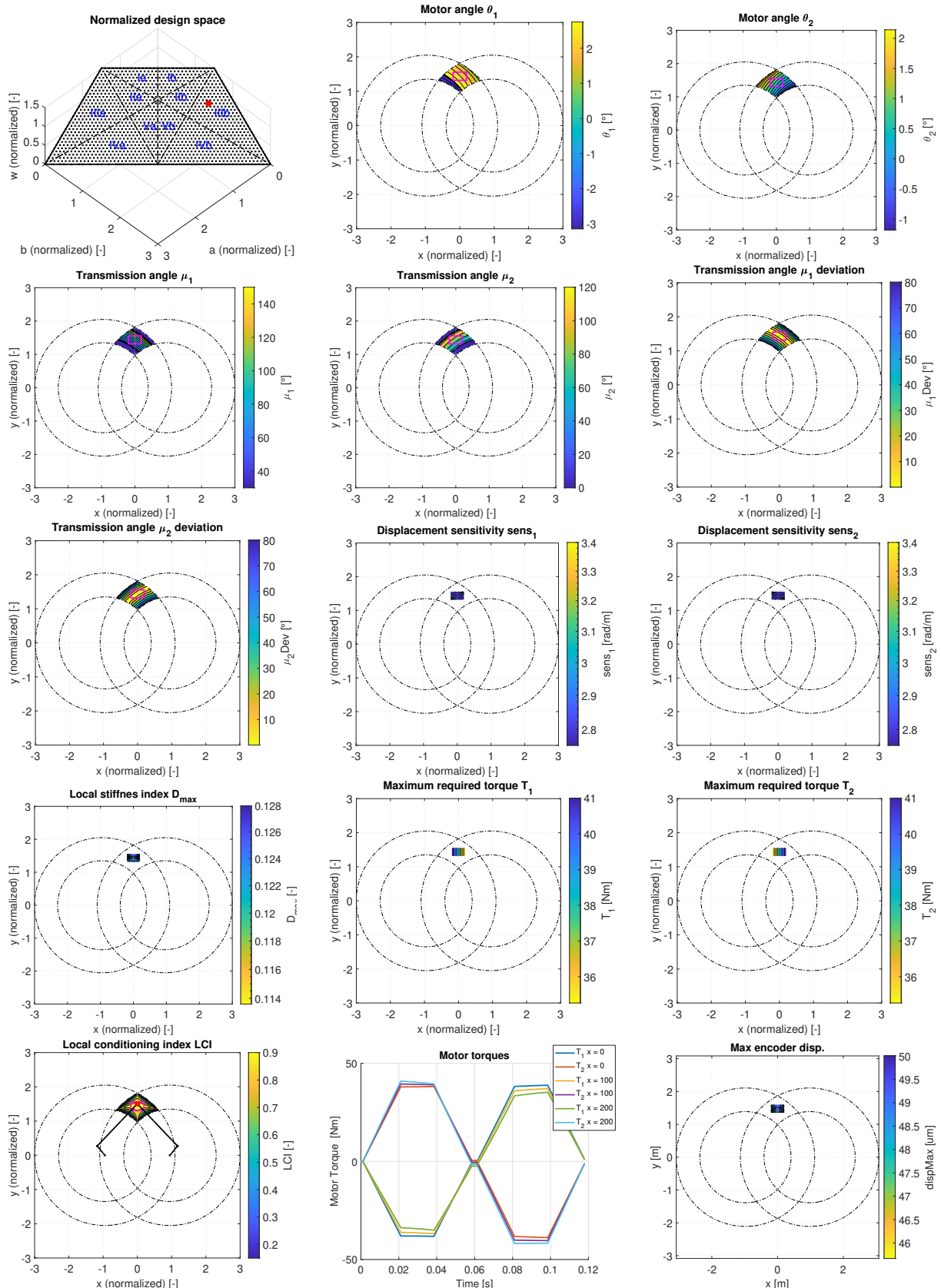


Figure A.2: Local performance indices plotted over the workspace of LS2.

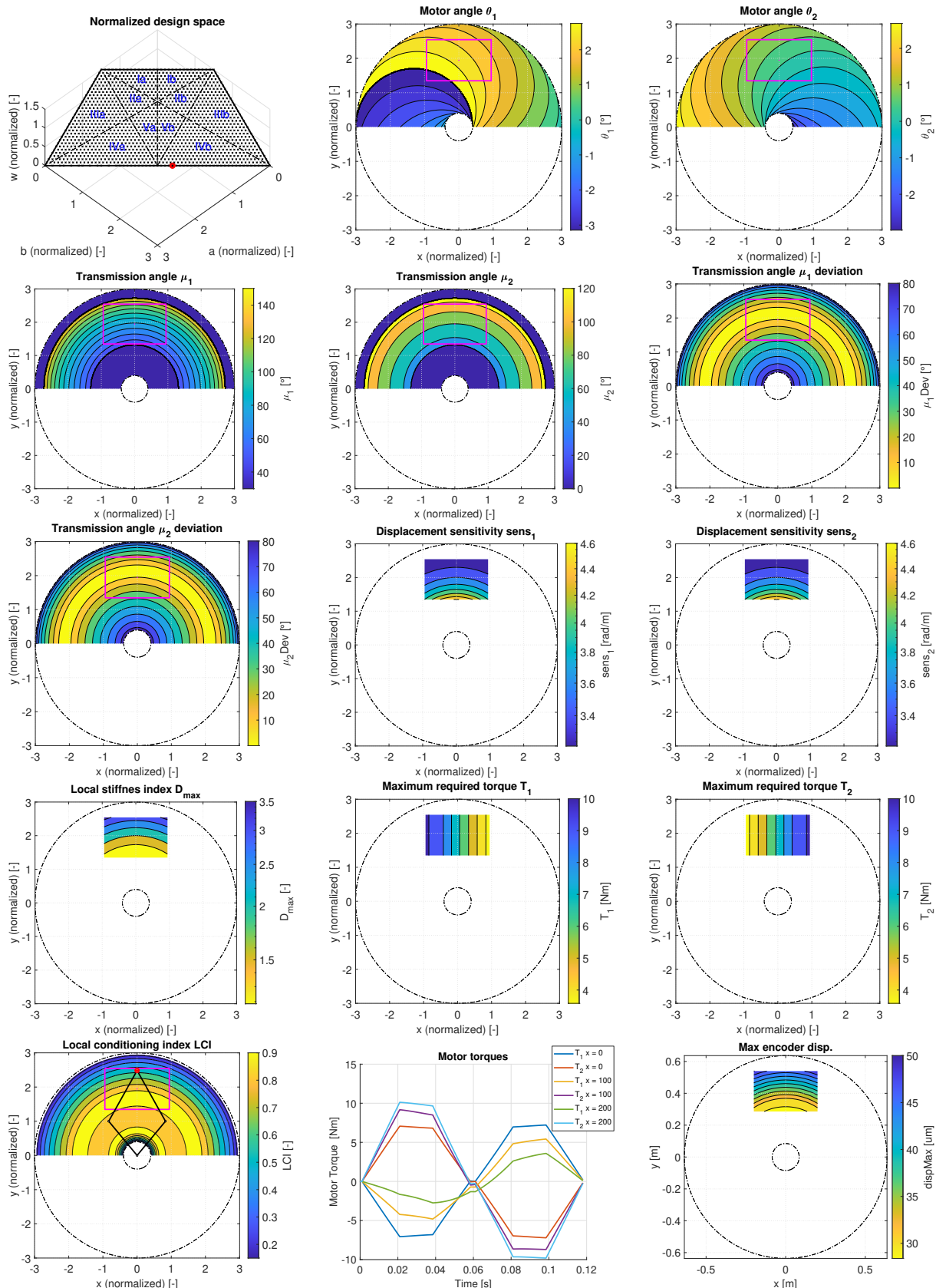


Figure A.3: Local performance indices plotted over the workspace of LS3.

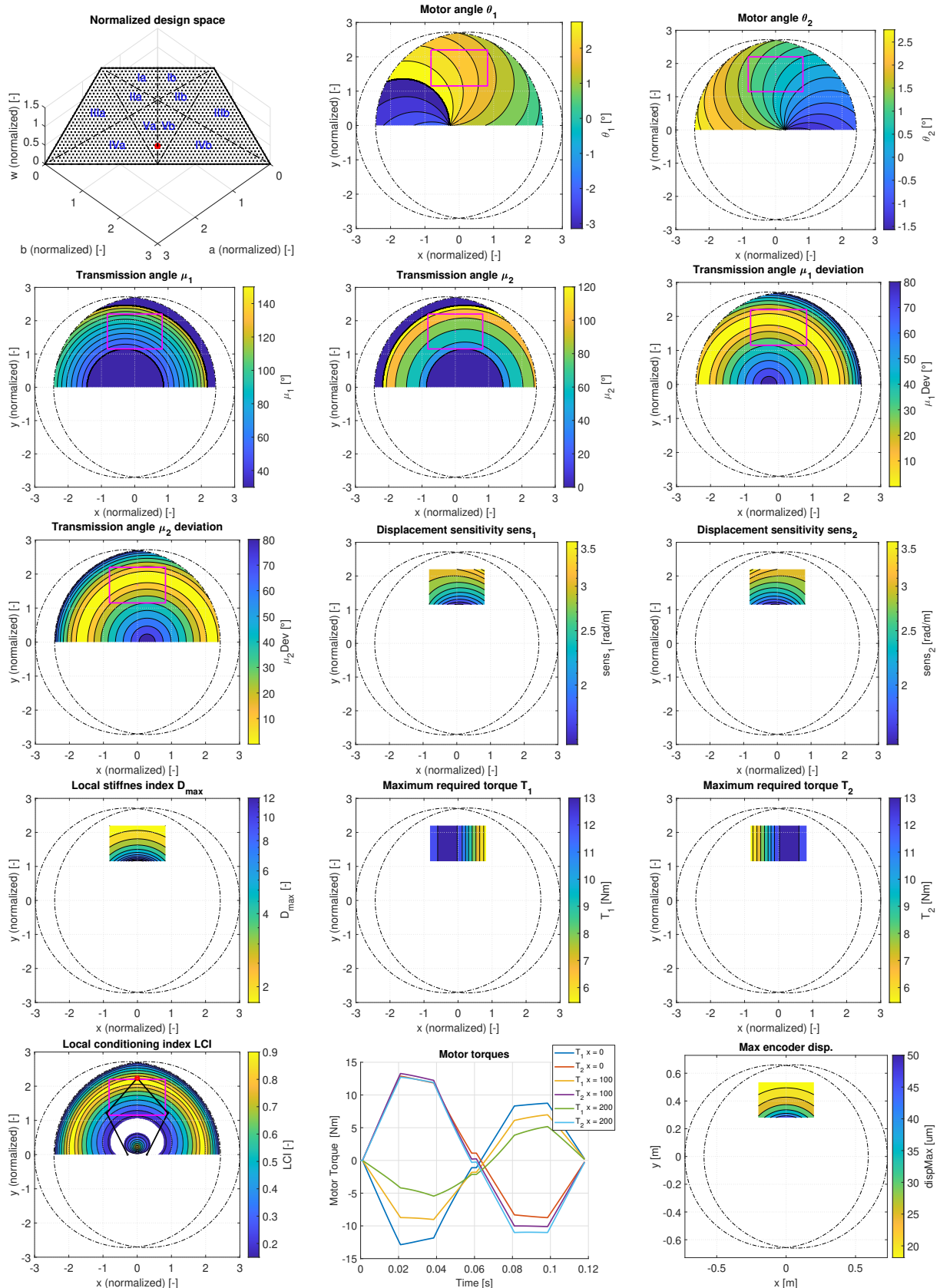


Figure A.4: Local performance indices plotted over the workspace of LS4.

B | Additional FEM results

B.1 | Mesh quality

- Global mesh size: maximum element size = 6 mm, minimum element size = 0.225 mm
- Leaf spring surface mesh refinement: maximum element size = 0.35 mm, minimum element size = 0.225 mm
- A plot of the mesh elements that have an aspect ratio greater than 4 can be seen in [Figure B.1](#). 5,534 of the 432,231 elements in the mesh (1.2%) have a poor aspect ratio.
- ~2.5 million DOFs, which fits within 20 GB of RAM.
- This simulation can be run in approximately 6 minutes on an Intel i7-9750H CPU (6 cores @ 2.6 GHz).

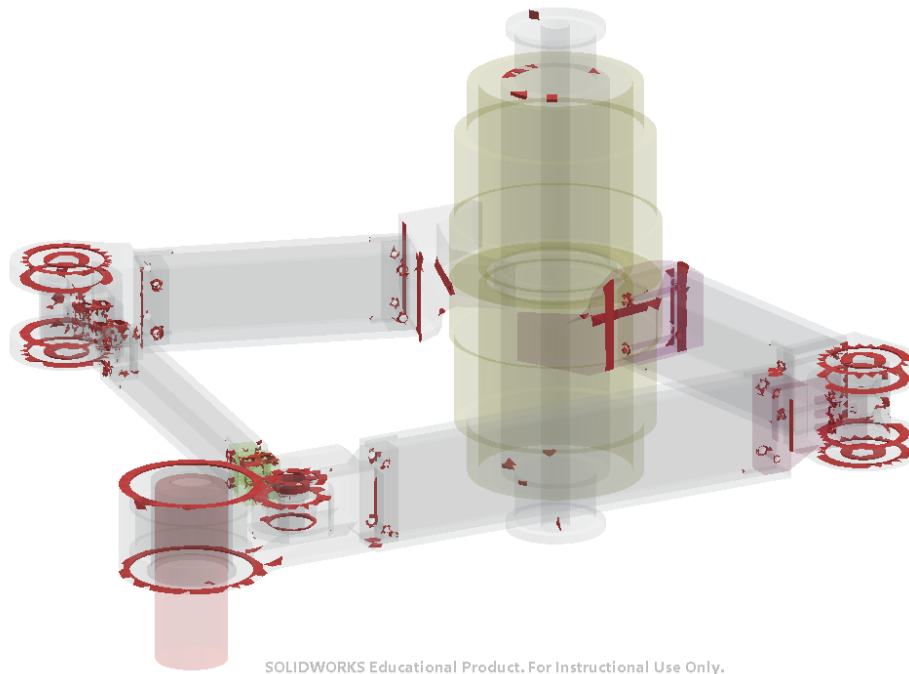
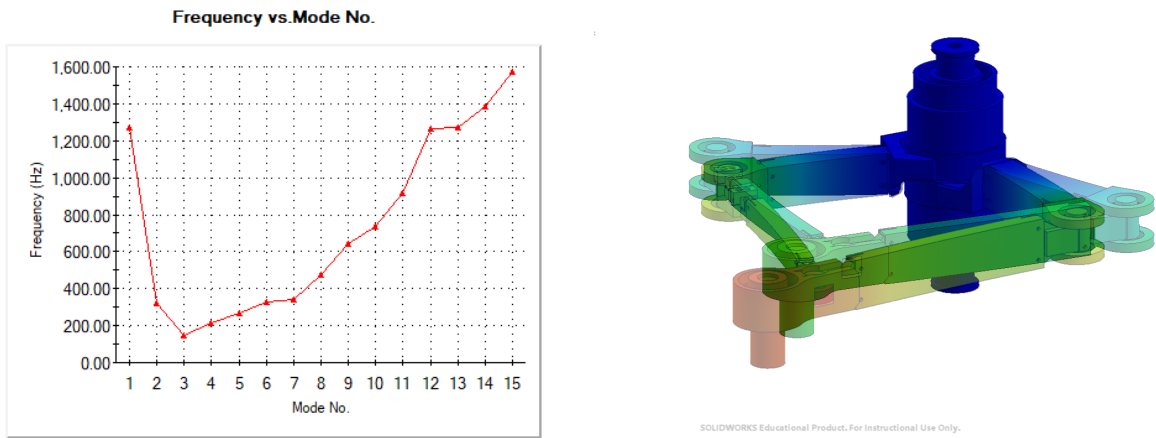


Figure B.1: Mesh elements with aspect ratio greater than 4. The circular regions of bad aspect ratio elements are caused by split lines required for the proper connection of various face-to-face connections.

B.2 | Erroneous modes

When requesting ten or more eigenmodes from the SOLIDWORKS Simulation Frequency studies created for the SCARA robot, a number of unexpected erroneous modes would be included in the results. These modes appear at the beginning of the mode list (i.e. they are the lowest numbered modes), while most of the time having a frequency higher than that of the expected (real) first mode. An example of such a situation can be seen in [Figure B.2a](#), where the frequency list from the centered pose simulation is displayed, as returned by SOLIDWORKS. In this case, the first three modes are erroneous. The mode shape of the first erroneous mode can be seen in [Figure B.2b](#). It can be observed that the deformation in this mode is entirely in the plane of the links, as if it were a rigid body mode (however it is at ~1300 Hz). The number of such modes has been observed to vary between one and three, even on different runs of the same study. A partial correlation with mesh size and fixture stiffness has been observed, however no direct cause for these erroneous modes could be identified. Moreover, when a reduced number of eigenmodes is requested from the solver (i.e. five), the erroneous modes disappear, while the expected modes and their frequencies remain unchanged. These modes have been manually removed from the results presented in the main text.



(a) Frequency vs. mode number plot, including 3 erroneous modes as modes 1-3. (b) Overlayed images of the extremes of the deformation in the first erroneous mode.

Figure B.2: Erroneous modes in the Frequency simulation for the centered pose.

B.3 | Modes 2-9 for the front-right pose

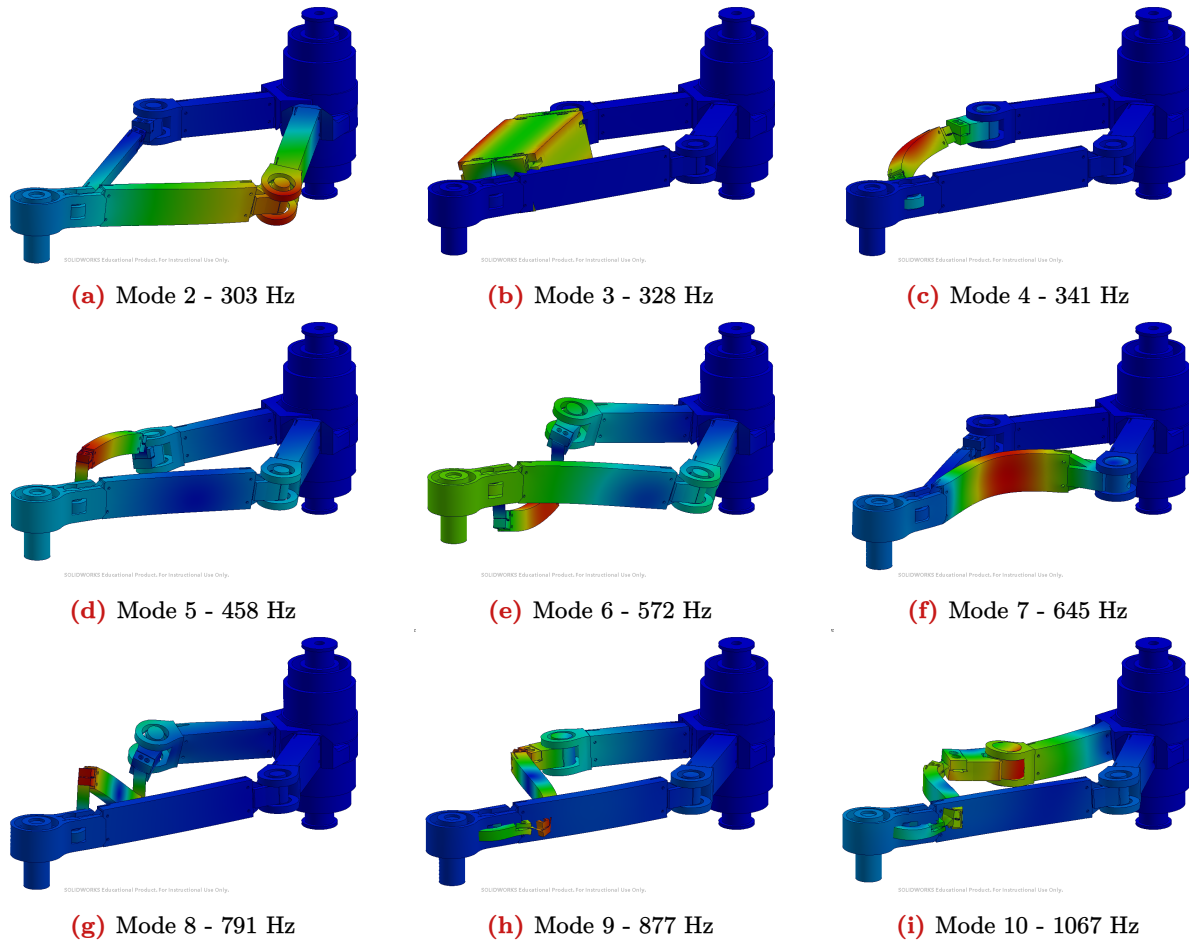


Figure B.3: Modes 2-10 in the front-right pose. The resultant displacement amplitude is plotted over the deformed model.